THE DUST-RADIO CONNECTION IN 3CR RADIO GALAXIES

SIGRID DE KOFF,[1,2] PHILIP BEST,[1] STEFI A. BAUM,[2] WILLIAM SPARKS,[2] HUUB RÖTTGERING,[1] GEORGE MILEY,[1] DANIEL GOLOMBEK,[2] FERDINANDO MACCHETTO,[2] AND ANDRE MARTEL[2]

ABSTRACT

We investigate dust in the nuclear regions of radio galaxies on the basis of 120 images of 3CR radio galaxies in the redshift range $0 < z < 0.5$, taken with the WFPC-2 on the *Hubble Space Telescope*. At least 40 of these radio galaxies show evidence for absorption due to clumpy dust features; a large range of morphologies is observed for these dust features, including disklike and filamentary structures. No difference in host galaxy properties was found between the radio galaxies with clumpy dust and those without. Where dust absorption is detected, the morphological properties of the dust depend strongly upon the Fanaroff & Riley (FR) classification of the source. The dust in FR I host galaxies is generally situated in sharply defined disks on small (< 2.5 kpc) scales, and for eight out of the nine FR I galaxies with dust disks, the radio source lies nearly perpendicular to the dust disk. In contrast, FR II host galaxies have dust that varies both in morphology and in linear size, and the correlation between the dust and radio orientation only exists (and less strongly) for the sources that have a significant mass of dust in disks within a distance of 2.5 kpc of the center of the galaxy. The derived dust masses also correlate with the FR type of the host galaxy: high masses of clumpy dust are not seen in FR I radio galaxies, while they are present in FR II radio galaxies. Further, FR I galaxies have derived dust masses that are typically larger than the dust masses found in a matched sample of radio-quiet ellipticals. We suggest that the observed differences between FR I and FR II radio galaxies are produced due to differences in their formation.

Subject headings: galaxies: ISM — galaxies: jets — galaxies: structure

1. INTRODUCTION

There is morphological evidence that gas and dust play a fundamental role in the production of a radio source. Two decades ago Kotanyi & Ekers (1979) found that seven low-redshift radio galaxies associated with elliptical galaxies all have disklike distributions of dust apparently aligned nearly perpendicular to the radio source. This raises a number of questions concerning the relationship between the dust and radio activity, such as the following. What is the origin of the dust? Is all of the dust settled in orbits around the galaxy nucleus, or is there dust distributed in filamentary structures throughout the galaxy? Do these results hold for all radio galaxies or do the properties of the dust depend upon the radio properties? For example, is there a difference between the dust properties of Fanaroff & Riley (1974, hereafter FR) class I and II sources, similar to the many differences seen between the emission line gas properties of these two classes of sources (e.g., Zirbel & Baum 1995, Baum, Zirbel, & O'Dea 1995, and references therein)? Are the properties of dust in radio-loud galaxies similar to those in radio-quiet galaxies?

In this paper, we present observations taken with the *Hubble Space Telescope* (*HST*), which provide new information about the role of dust in radio galaxies and allow many of these questions to be tackled. We used the sample of 3CR radio galaxies with redshifts $z < 0.5$ from the *HST* Snapshot survey of 3CR radio sources. The high resolution of the *HST* images allows us to observe the dust in greater detail and on smaller physical scales than ever before and for the first time to carry out a statistical survey of the morphol-ogies of dust structures in the nuclear regions of radio galaxies out to a redshift of ~ 0.5. It is in the nuclear regions where the interaction between radio source and dust is most likely to be important. In determining physical properties using distance, we assume $H_0 = 75$ km s^{-1} Mpc^{-1} and $\Omega = 1.0$ throughout this paper.

2. THE DATA; SELECTION AND ANALYSIS

2.1. *Observations and Reduction*

Our data set is a subset of the *Hubble Space Telescope* 3CR snapshot survey, conducted using the Wide Field and Planetary Camera 2 (WFPC-2) in snapshot mode (typical exposure time 300 s). The initial snapshot program was based on the revised 3CR sample as defined by Bennett (1962): $S(178) > 9$ Jy and $\delta > -5$, with the additional constraint that $b > 10°$. The completeness properties of the 3CR are discussed by Laing, Riley, & Longair (1983). Some targets were excluded from the program because of duplications with other *HST* programs, and several more were not observed because of scheduling practicalities. For the current paper we consider all of the radio galaxies with a redshift of less than 0.5 that were observed during the program. In this redshift range the observations are 87% complete, resulting in a sample of 120 radio galaxies.

All of the *HST* snapshot images were obtained using a red broadband filter centered near 7000 Å (F702W). This filter gives maximum sensitivity and includes continuum and in some cases line emission. The images have an angular resolution of $\sim 0″.1$. The processing and reduction of the images are described by de Koff et al. (1996; $0.1 < z < 0.5$), and Martel et al. (1999; $z < 0.1$).

We conducted a literature search for radio maps having a resolution comparable to that of the *HST* data. Sources for which no such data existed were observed with the VLA (A and B array, at 3.6 cm) in a "VLA 3CR Snapshot

[1] Leiden Observatory, Postbus 9513, 2300 RA, Leiden, The Netherlands.
[2] Space Telescope Science Institute, 3800 San Martin Drive, Baltimore, MD 21218.

Survey." The resultant radio maps were used to make morphological comparisons with the *HST* images. The "VLA 3CR Snapshot Survey" data will be described and discussed elsewhere.

2.2. *Selection of Dusty Galaxies*

In the absence of color information, the sample of radio galaxies displaying dust absorption was selected on the basis of morphological features. These morphological features range from extended obscuration of light to small disturbances in the isophotes near the nucleus.

In order to identify faint dust features, smooth galaxy models were first derived by fitting elliptical isophotes to the original galaxy images, using the NOAO Image Reduction and Analysis Facility (IRAF) software package. The task "ellipse" was used to fit the elliptical isophotes; this task is based on a method (described in detail by Jedrzejewski 1987) which uses all of the data points in the image and calculates the center, ellipticity and position angle of the elliptical isophotes at different radii, with their uncertainties. Next, the task "bmodel" was used to create a two-dimensional model image using the data from the table created by the "ellipse" task. This galaxy model was then subtracted from the original image, and if residual features were detected in the map (e.g., due to obscuration by dust or foreground globular clusters), then the model fitting procedure was repeated, this time with those residual features masked out. The resultant fitting parameters were used to construct the final two-dimensional model images. Further details of this method, and the detailed results of the galaxy fitting, will be described in a follow-up paper. The conclusions drawn in this paper are not dependent upon the precise details of the galaxy modeling.

Galaxy models could be constructed for 94 of the 120 sources. For the remainder it was not possible because of a peculiar galaxy morphology. In a number of cases, this was due to strong dust absorption of galaxy light already easily visible; in other cases it was due to the galaxy being too elongated, having bright tails of emission, or having a nearby bright star or companion galaxy. Where a galaxy model could be constructed, the original image was divided by the galaxy model to obtain a "model absorption map" which represents the spatial distribution of absorption on the assumption that the brightness distributions are ellipsoidal. Although one must be cautious about interpreting such "model absorption maps" as purely being due to dust absorption, in the absence of color information it is illustrative to carry out such an analysis. In this way, one can hope to obtain information about systematics in the morphology of the nuclear dust.

Our limit for detecting a patch of dust was set such that at least 20% of the light had to be absorbed over a minimum extent of 3 × 3 pixels. The behavior of this filter does not correspond to a precise dust mass detection limit as a function of redshift, since the limit depends upon the manner in which the dust is clumped (uniformly distributed dust will be missed) and the surface brightness of the emission underlying the dust. However, it is a clear and (most importantly) repeatable definition which will detect significant dust absorption features without selecting noise features. According to this definition, 22 of the model absorption maps showed clear dust features.

For the remaining 26 sources for which no model absorption maps could be made, 18 showed clear absorption features visible directly from the original *HST* image. These galaxies are therefore also included in the sample (these are 3C 20, 3C 46, 3C 52, 3C 83.1, 3C 136.1, 3C 171, 3C 173.1, 3C 180, 3C 196.1, 3C 268.2, 3C 274.1, 3C 275, 3C 284, 3C 303.1, 3C 306.1, 3C 315, 3C 353, 3C 452). The selection of these galaxies is, unavoidably, based upon more qualitative criteria. In total, then, we find that 40 of the 120 radio galaxies in our $z < 0.5$ sample have morphological features indicative of clumpy dust in the nuclear regions. Although the selection of the sample is based on somewhat qualitative criteria, we are confident that almost all of the 40 selected galaxies have definite dust features. However, the 80 objects not included in the sample are also likely to contain dust, distributed more uniformly or clumped in masses below our detection limit.

The "model absorption maps" of the galaxy central regions (or original *HST* images if no absorption map could be made) are presented in Figures 1–40 for the objects that show clear evidence for dust absorption. The gray-scale images of the data from which the maps were derived can be found in de Koff et al. (1996) and Martel et al. (1999). In the figures a scale bar indicates the linear scale. The sample of radio galaxies in which we observe clear dust obscuration spans a redshift range of $z = 0.0031$ for 3C 272.1 to $z = 0.480$ for 3C 275. Table 1 lists this sample with their redshifts and a number of important parameters.

Together with the model absorption maps, in many cases we show the *HST* images with the radio contours superposed and a large-scale radio map for morphological comparison. Some radio properties of the sources are summarized in Table 1. References to the radio data are given in parentheses in the figure captions.[3]

2.3. *Descriptions of Individual Sources*

The dust features in all the individual radio galaxies in the sample are described below in right ascension order.

3C 20, $z = 0.174$.—The original image (Fig. 1) shows possibly a dust disk and two cones of emission. Because of the complex structure of the source it was not possible to fit ellipses to the isophotes. The large-scale FR II class radio structure is aligned roughly perpendicular to the proposed dust lane.

3C 31 (NGC 383), $z = 0.0167$.—This galaxy is the brightest in a chain of eight galaxies and appears to be interacting with a close ($\approx 30''$) companion NGC 382 (Arp 331). Low surface brightness emission connects the two galaxies. Figure 2 shows a spectacular face-on disk in which as many as eight dust strands are visible, with a typical projected separation of about 70 pc (see also Verdoes Kleijn et al. 1999). The disk shows more absorption on the southwestern side than the other, presumably indicating the orientation of the disk with respect to the observer; from the axial ratio (b/a) of the dust disk, the southwestern region can then be taken as pointing toward the observer with an inclination of arccos $(b/a) \approx 41°$ with respect to the plane of the sky. This

---

[3] (1) Laing, unpublished; (2) 3CRR atlas; (3) Kronberg, unpublished; (4) O'Dea, unpublished; (5) Pedlar et al. 1990; (6) Laing, unpublished; Heckman, van Breugel, & Miley 1984; (7) Leahy & Perley 1991; (8) Mack et al. 1997; (9) Baum et al. 1988; (10) Laing & Bridle 1987; (11) Leahy, Pooley, & Riley 1986; (12) Akujor et al. 1991; (13) Leahy et al. 1997; Wrobel, Condon, & Machalski 1998; (14) Leahy & Williams 1984; (15) Ge & Owen 1994; (16) Black et al. 1992; (17) Christiansen, unpublished; (18) Owen, unpublished; (19) VLA Snapshot Survey.

TABLE 1

DUST IN RADIO GALAXIES, SOME OPTICAL AND RADIO PROPERTIES

3CR (1)	z (2)	M_R (3)	CC (kpc) (4)	$\log_{10} D$ (5)	P.A. (deg) (6)	Jet (7)	FR Type (8)	Radio Morphology (9)
3C 20.	0.174	-19.0	13	2.24	101	1,?	II	Double
3C 31.	0.0167	-22.1	9	2.10	159	2	I	Wiggles
3C 46.	0.4373	-21.9	7	3.10	68		II	Double
3C 52.	0.2854	-21.0	23	2.44	102		II	X shape
3C 83.1	0.0255	< -23.0	0.75	2.50	86	2	I	NAT
3C 84.	0.0172	< -23.4		2.23	160	2	I	Amorphous
3C 88.	0.0302	-21.0		2.12	56		I	Double
3C 136.1......	0.064	-19.4	2	2.76	106	...	II	X shape
3C 171.	0.2384	-20.5	10	2.14	100	2	II	H shape
3C 173.1......	0.292	-21.6	53	2.51	17	1	II	Sym. double
3C 180.	0.22	-20.5	40		7			Sym. double
3C 196.1......	0.198	-20.3	11	1.17	47		II	Double
3C 223.1......	0.1075	-20.8		2.39	15	?	II	X shape
3C 236.	0.0989	-21.9		3.67	117		II	Double core, double
3C 264.	0.0208	-21.6		1.41	31	1,?	I	Wiggle
3C 268.2......	0.362	-21.3	69	2.81	21			Sym. double
3C 270.	0.0073	< -21.8		1.78	86	2	I	Double, one-sided wiggle
3C 272.1......	0.0031	-21.1		1.05	176	2	I	S shape
3C 274.1......	0.422	-20.8	49	3.06	76		II	Double
3C 275.	0.48	-21.6	...	1.62	51		II	Double
3C 284.	0.2394	-21.3	...	2.91	87	...	II	Double
3C 293.	0.0452	-21.7		2.33	92		II	Double core
3C 296.	0.0237	-22.7		2.31	37	2	I	Two-sided jet
3C 303.1......	0.267	-21.0	55	0.96	132		II	Double
3C 305.	0.041	-22.4		1.02	45	1	II	H shape
3C 306.1......	0.441	-21.5	12	2.86	180		II	Sym. double
3C 315.	0.1083	-20.0	12		25		I	X shape
3C 321.	0.096	< -22.4	5	2.75	120	1	II	Sym. double
3C 326.	0.0895	-21.1		3.31	81		II	Sym. double
3C 327.	0.1039	-20.8		2.54	100	?,?	II	Double
3C 338.	0.0298	< -22.6	5	1.81	89		I	Odd
3C 353.	0.0304	-20.3		2.20	84	2	I	Double
3C 357.	0.1664	-21.0	30	2.42	111		II	Double
3C 403.	0.059	< -22.6		2.39	64	1	II	X shape
3C 430.	0.0541	-20.4		2.00	35	...		Sym. double
3C 433.	0.1016	-20.7	13	2.06	166	1	II	Amorphous
3C 436.	0.2145	-20.6	57	2.64	173	1	II	Sym. double
3C 449.	0.0171	-21.1		2.63	8	2	I	Weak wiggles
3C 452.	0.0811	< -21.8		2.60	80	2	II	Sym. double
3C 465.	0.0293	< -22.3	7	2.31	122	2		WAT

NOTES.—Col. (2), redshift; col. (3), absolute R-band magnitude; col. (4), distance to the closest companion galaxy in kpc; col. (5), logarithm of the largest linear size (in kpc) of the radio source; col. (6), position angle of the jet/large-scale radio source; col. (7), presence of radio jets; one or two-sided; col. (8), Fanaroff-Riley type; col. (9), radio morphology description.

agrees with the result of Fraix-Burnet, Golombek, & Macchetto (1991), who derived the inclination using the same method.

The large-scale radio map shows well-defined radio jets with several sharp bends within a projected distance of 100 kpc from the galaxy. Figure 2 shows the innermost part of the radio jet superposed on the *HST* image; the radio map shows a bright radio core and a gap between the core and the jet corresponding to about the projected size of the dust disk. No direct evidence is found for a relation between the morphology of the radio source and the dust.

3C 46, $z = 0.4373$.—No model absorption map could be made for this galaxy because of a nearby companion galaxy, of similar size and brightness as 3C 46, at a distance of ~ 6.5 kpc to the north, that strongly affects the isophotes of 3C 46. Nevertheless, Figure 3 shows a convincing example of dust at higher redshift, with a dust lane lying right across

the nucleus. The large-scale radio structure shows a core and two hot spots on one line, nearly perpendicular to the dust lane.

3C 52, $z = 0.2854$.—The original *HST* image (Fig. 4) shows another convincing case of an obscuring dust disk at a relatively high redshift. The radio map shown illustrates that the radio axis is approximately perpendicular to the dust disk. Deeper radio maps show that the extended radio emission of this source is X-shaped.

3C 83.1 (NGC 1265), $z = 0.0255$.—This galaxy is a member of the Perseus cluster. It shows a sharp, well defined edge-on disk (Fig. 5), although a nearby star at $3''$ distance from the galaxy core makes modeling of the galaxy impossible.

The radio map shows a "narrow angle tail" radio structure, with several wiggles in the radio jet before the large-scale radio tail bends toward the northwest. Figure 5 shows
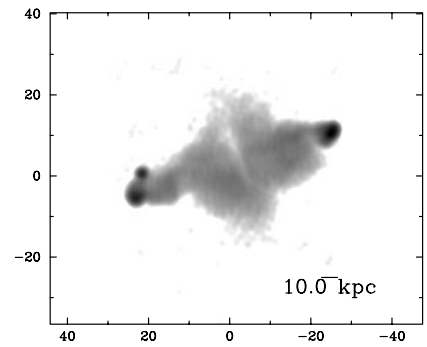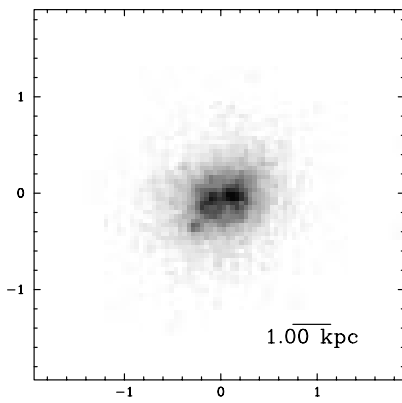
Fig. 1.—3C 20; *left*, original *HST* image; *right*, large-scale radio map (1)

that the inner jet and dust disk are oriented almost perpendicular to each other.

3C 84 (NGC 1275), z = 0.0172.—3C 84 is the central galaxy of the Perseus cluster and is believed to be a colliding system. The map (Fig. 6) shows filamentary dust structures throughout the galaxy. The dust extends out to 17 kpc, the most extended dust structure observed in this sample. In the map two arms of emission can also be seen east of the dust. These may be signs of recent interaction with another galaxy (e.g., NGC 1272), or a projection of a small spiral galaxy on top of 3C 84. A VLA/MERLIN map of 3C 84 shows a core and a jet inside a 10 arcminute radio halo (Pedlar et al. 1990). The radio map in Figure 6 shows the extended amorphous radio source.

3C 88, z = 0.0302.—The "model absorption map" of 3C 88 (Fig. 7) shows a faint dust feature very close to the nucleus of the galaxy. The associated FR I class radio source shows a prominent core, a one-sided radio jet, and two lobes of faint diffuse emission (Baum et al. 1988).

3C 136.1, z = 0.064.—Figure 8 shows the original *HST* image. The galaxy has a very elongated dumbbell shape, which prevented a model absorption map being made. The nucleus of the galaxy is also dumbbell in shape, presumably due to obscuration by a dust lane, but with the elongation at right angles to that of the host galaxy. Approximately 1.5 kpc SSE of the nucleus there is a feature that may be the nucleus of an interacting galaxy. The extended radio source is X-shaped (Leahy & Williams 1984).
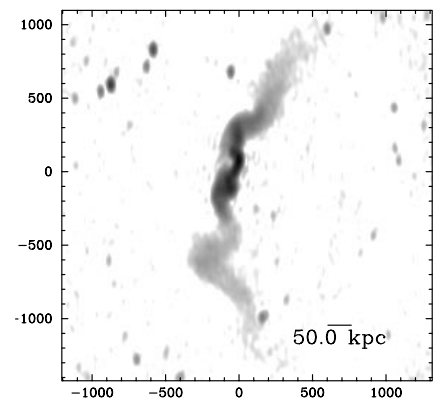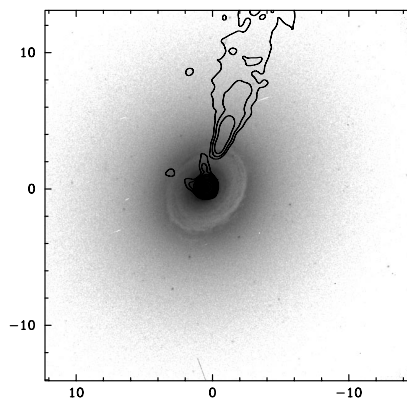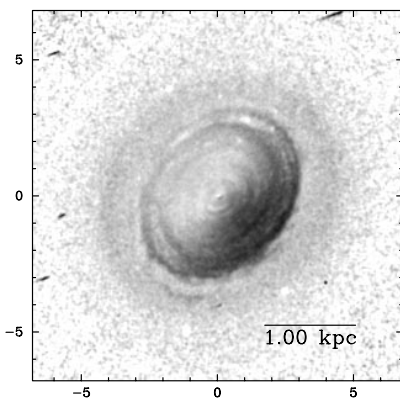
Fig. 2.—3C 31; *left*, absorption map; *middle*, *HST* image with radio contours superposed (19); *right*, large-scale radio map (2)
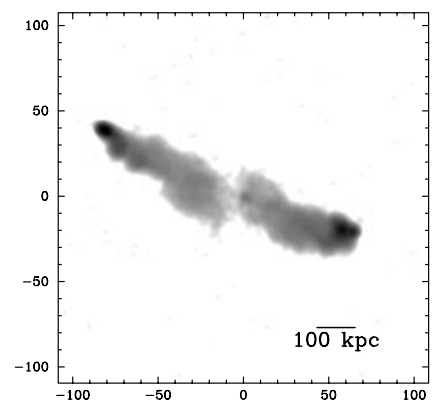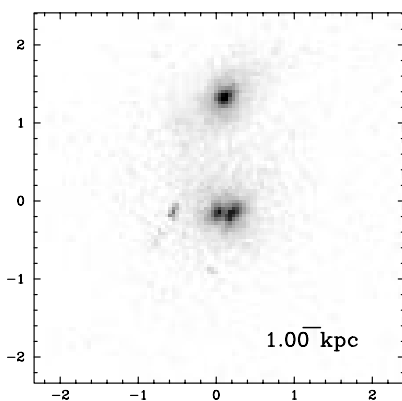
Fig. 3.—3C 46; *left*, original *HST* image; *right*, large-scale radio map (2, 3)

Fig. 4.—3C 52; *left*, original *HST* image; *right*, large-scale radio map (19)

3C 171, $z = 0.2384$.—This galaxy has an elongated nucleus that seems to be partly obscured by dust (Fig. 9). The contribution to the *HST* image from line emission is large. The optical emission of the galaxy is strongly elongated along the radio axis, and the emission line gas of this source appears to be interacting strongly with the radio source (see Heckman, van Breugel, & Miley 1984). The dust seems to be in a much more stable configuration, in a lane perpendicular to the radio axis. The radio source has an H shape with the horizontal bar in east-west direction.

3C 173.1, $z = 0.292$.—Figure 10 shows a nucleus partly obscured by a dust lane. The large-scale radio source shows a core and two hot spots on one line in roughly north-south direction, perpendicular to the dust lane.

3C 180, $z = 0.22$.—This boxy galaxy has a disturbed nucleus (Fig. 11), consisting of two or three separate emis-
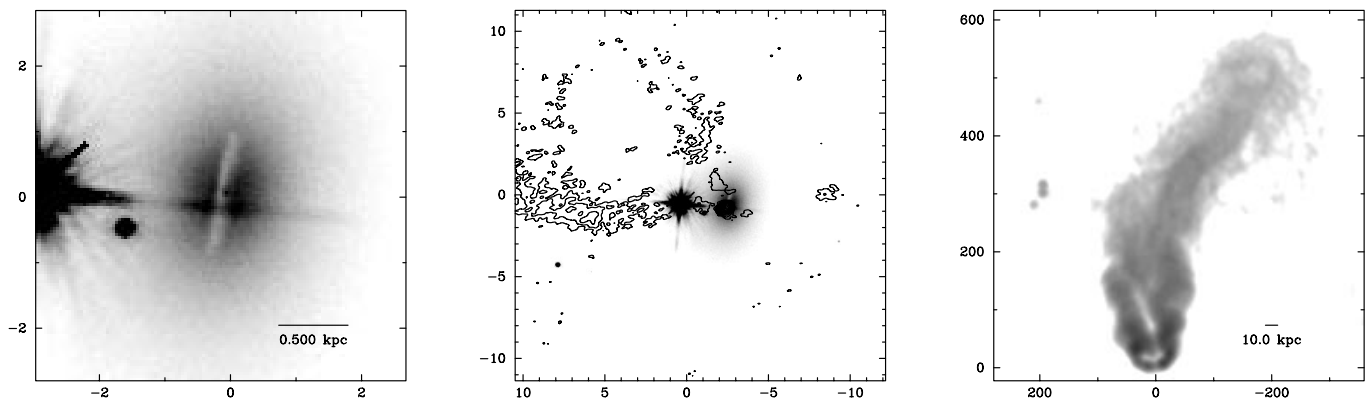
Fig. 5.—3C 83.1; *left*, original *HST* image; *middle*, *HST* image with radio contours superposed (19); *right*, large-scale radio map (4)

Fig. 6.—3C 84; *left*, absorption map; *right*, large-scale radio map (5)
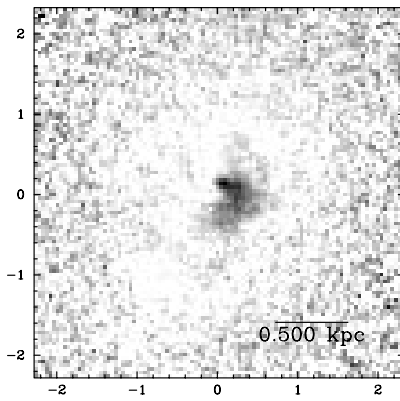
Fig. 7.—3C 88; Absorption map

sion regions, which prevented the construction of galaxy model isophotes. It seems likely that the nuclear morphology is determined by dust. The extended radio structure is perpendicular to the proposed dust disks.

3C 196.1, z = 0.198.—This extremely elongated galaxy (Fig. 12) has part of the nucleus seemingly obscured by dust. No modeling was possible because of the extreme elongation of the galaxy. The radio map shows a core-jet structure, with the jet oriented along the major axis of the optical emission and perpendicular to the assumed dust disk.

3C 223.1, z = 0.1075.—The image (Fig. 13) shows a large-scale double dust disk. There are indications of dust arms close to the nucleus of the galaxy. The radio map presented shows that the axis of the radio emission is oriented along, rather than perpendicular to, the dust disk. The extended radio emission is X-shaped (Black et al. 1992).

3C 236, z = 0.0989.—The absorption map (Fig. 14) shows a dust disk on scales of a few kpc. Closer to the nucleus (~ 1 kpc) there is another dust feature that seems to be connected to the larger disk by a strand of dust going from one
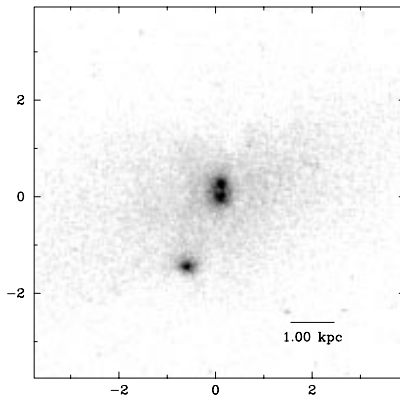
Fig. 8.—3C 136.1; Original *HST* image
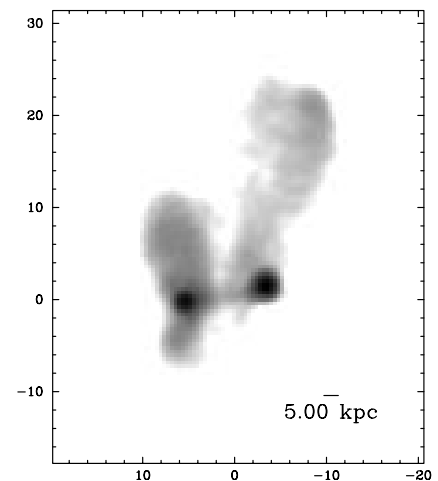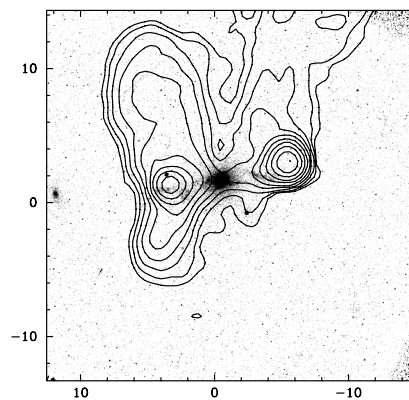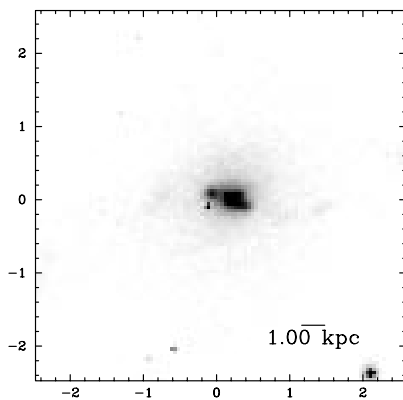
Fig. 9.—3C 171; *left*, original *HST* image; *middle*, *HST* image with radio contours superposed (6); *right*, large-scale radio map (6)
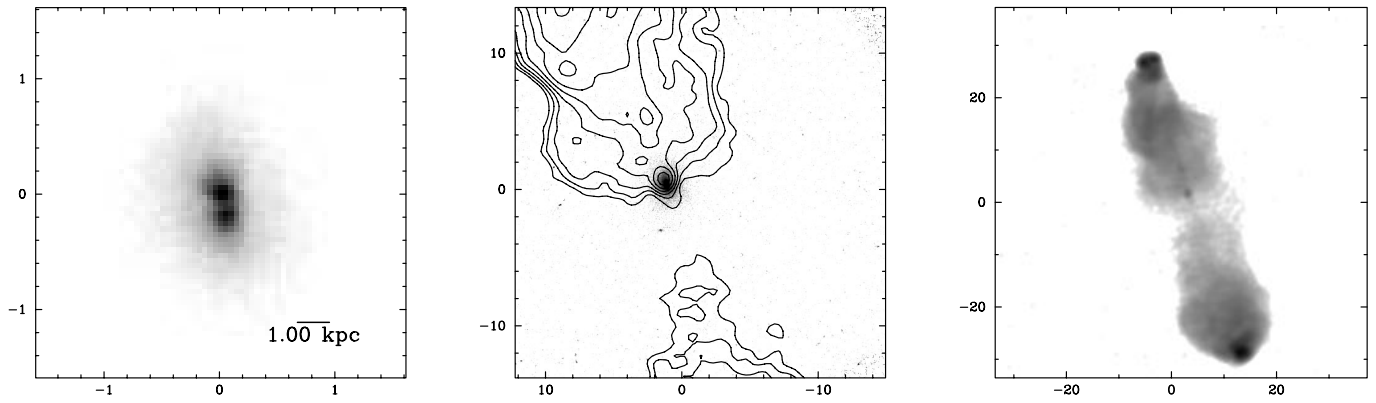
FIG. 10.—3C 173.1; *left*, original *HST* image; *middle*, *HST* image with radio contours superposed (7); *right*, large-scale radio map (7)

to the other. This is the largest radio source known (Barthel et al. 1985). The radio structure of this source shows two long straight lobes and hotspots, and close to the radio core, colinear with this, a compact–steep-spectrum–like radio source extending over the inner $1\overset{''}{.}5$.

3C 264 (NGC 3862), $z = 0.0208$.—This object lies in a dense part of the cluster Abell 1367. Figure 15 shows a face-on dust disk with an optical jet projected on it. The

dust disk appears to have its physical boundary at the same distance from the nucleus as the projected optical jet. A radio jet coincides with the optical jet. Baum et al. (1997) have described in detail the relation between the optical jet, dust disk and radio jet.

3C 268.2, $z = 0.362$.—This galaxy is extremely elongated (Fig. 16), as a result of which it was not possible to make a model absorption map. However, from the images it
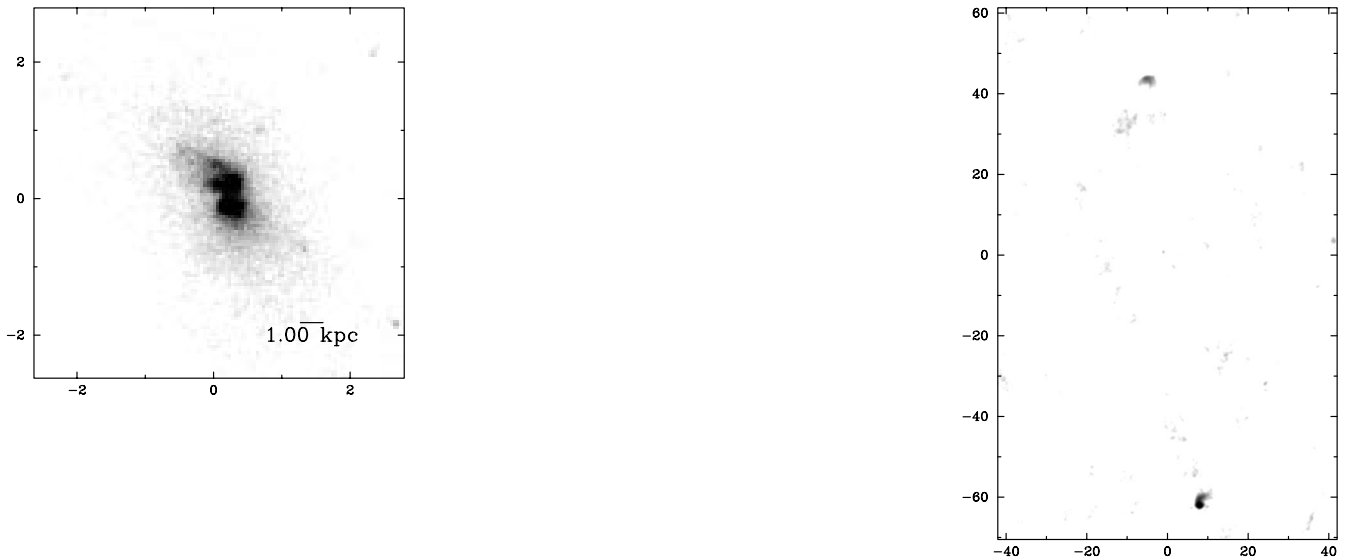
FIG. 11.—3C 180; *left*, original *HST* image; *right*, large-scale radio map (19)
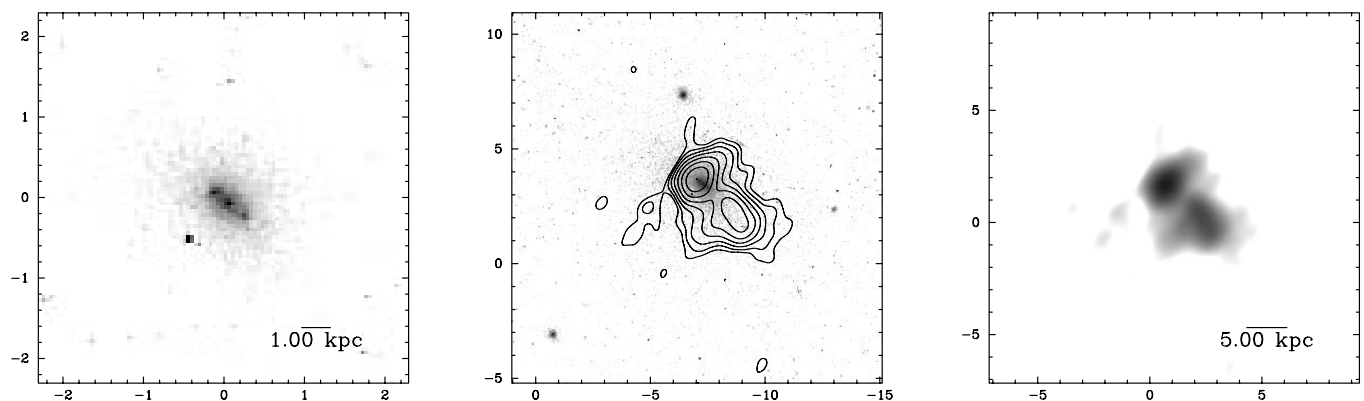
FIG. 12.—3C 196.1; *left*, original *HST* image; *middle*, *HST* image with radio contours superposed (19); *right*, large-scale radio map (19)
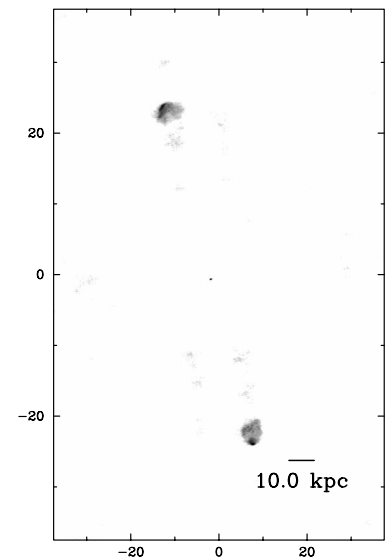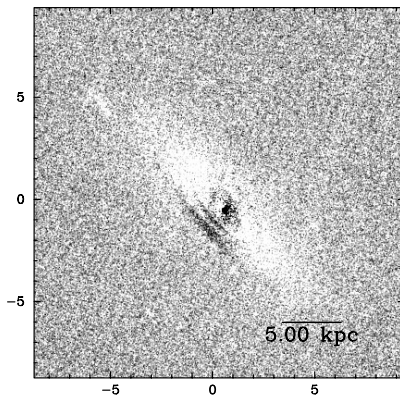
FIG. 13.—3C 223.1; *left*, absorption map; *right*, large-scale radio map (19)

appears that part of the nucleus is obscured by dust. The large-scale radio source is a double (Neff, Roberts, & Hutchings 1995) with a position angle of 21°, thus *misaligned* with the major axis of the optical galaxy.

3C 270 (NGC 4261), z = 0.0073.—This is a well known radio source in the Virgo cluster. The model absorption map (Fig. 17) shows a small, sharply defined, nearly edge-on disk. This dust disk has been previously observed with *HST*

and discussed in detail by Jaffe et al. (1996). The radio source shows two jets almost perpendicular to the disk. The eastern lobe bends to the south.

3C 272.1 (NGC 4374, M84), z = 0.0031.—This galaxy is an elliptical in the Virgo cluster, in which dust was first detected long ago (e.g., Hansen et al. 1985). The model absorption map (Fig. 18; see also Verdoes Kleijn et al. 1999) shows a dust lane divided into several distinct strands.
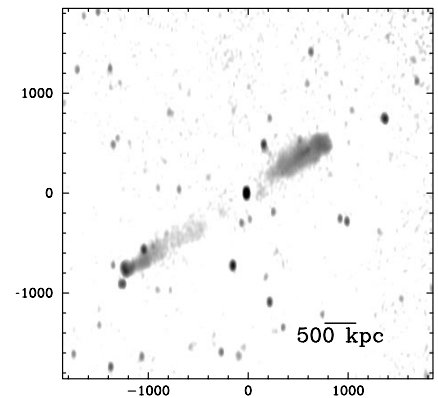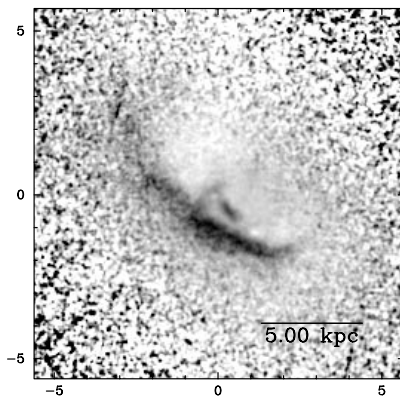
FIG. 14.—3C 236; *left*, absorption map; *right*, large-scale radio map (8)
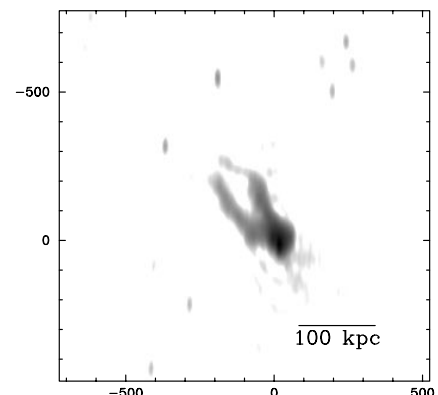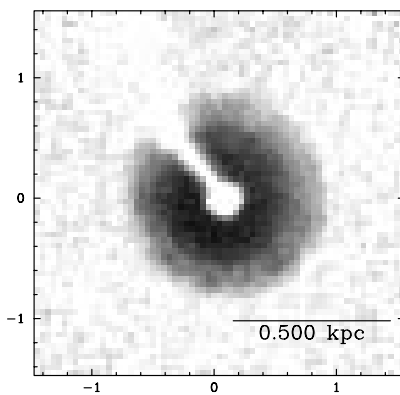
FIG. 15.—3C 264; *left*, absorption map; *right*, large-scale radio map (2)
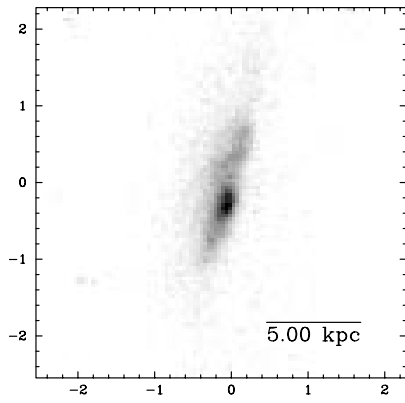
Fig. 16.—3C 268.2; Original *HST* image

There are bends in each strand that mimic each other. The projected length extends out to almost 1 kpc, and the dust appears to flair out at the end.

The large-scale structure of the radio source shows an S shape. The dust lanes make a right angle with the radio jet. Apart from this, there seems to be no correlation between the morphology of the large-scale radio structure and the morphology of the dust.

3C 274.1, $z = 0.422$.—Because of the low signal-to-noise ratio of this image, it was not possible to fit ellipses to the galaxy. However, Figure 19 shows that the galaxy has a faint nucleus, the center of which is obscured by dust.

3C 275, $z = 0.48$.—This galaxy, shown in Figure 20, has a nucleus that seems to be partly obscured by a dust lane. On a large scale, two tails of emission extend perpendicular to the dust lane. These features may be signatures of a violent past, like a merging event. The radio map (Mantovani et al. 1992) shows a double source positioned almost in the direction of the emission tails, perpendicular to the dust lane.

3C 284, $z = 0.2394$.—The original *HST* image (Fig. 21) shows an object similar to 3C 275. The large-scale radio structure is positioned in the same direction as the arms of optical emission, perpendicular to the dust lane.

3C 293, $z = 0.0452$.—The model absorption map (Fig.
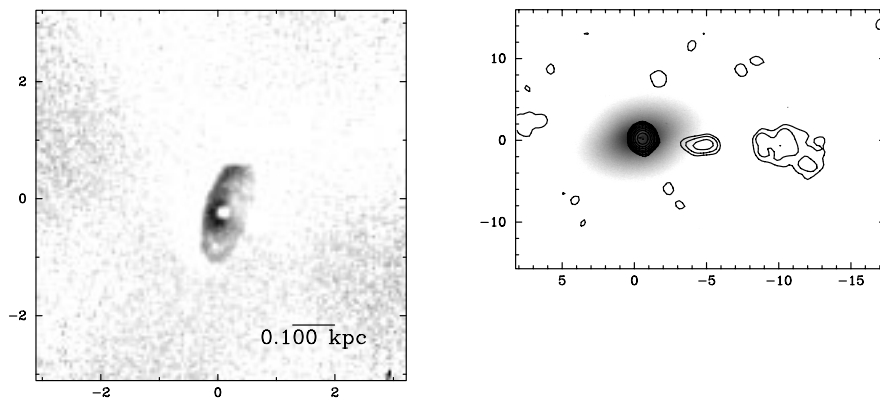
Fig. 17.—3C 270; *left*, absorption map; *right*, *HST* image with radio contours superposed (9)
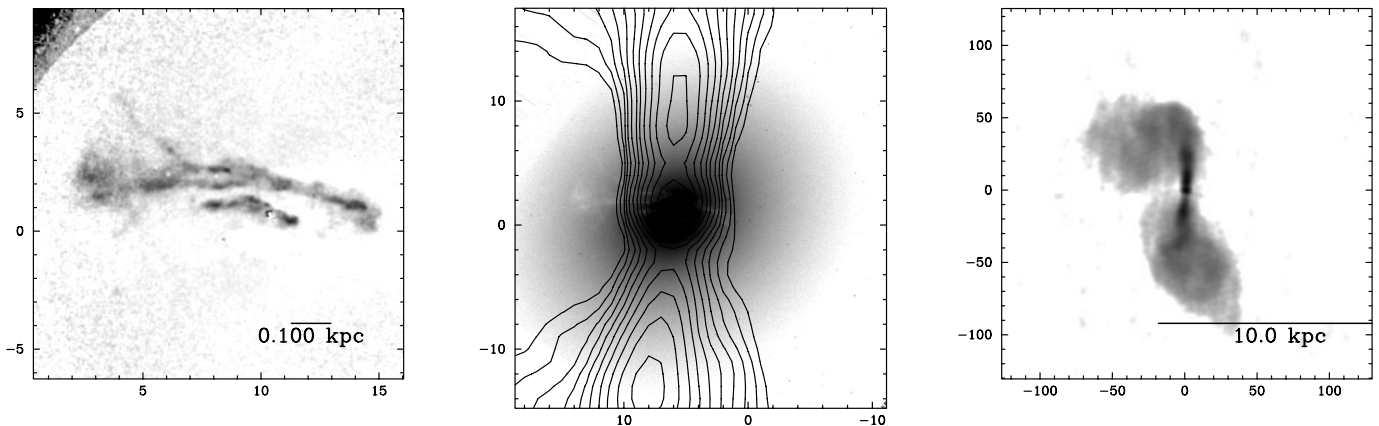
Fig. 18.—3C 272.1; *left*, absorption map; *middle*, *HST* image with radio contours superposed (10); *right*, large-scale radio map (10)
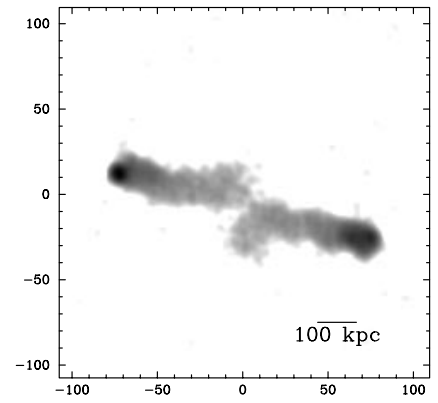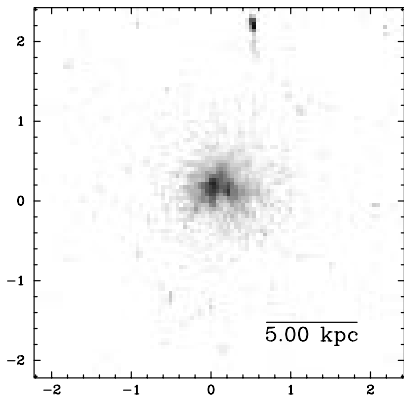
Fig. 19.—3C 274.1; *left*, original image; *right*, large-scale radio map (11)
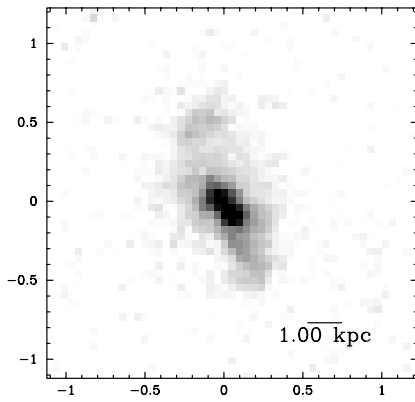
Fig. 20.—3C 275; Original *HST* image
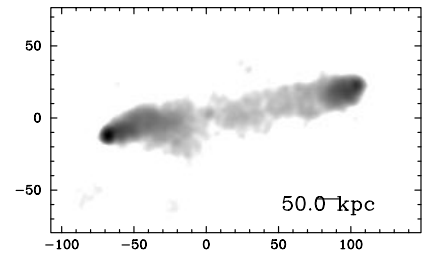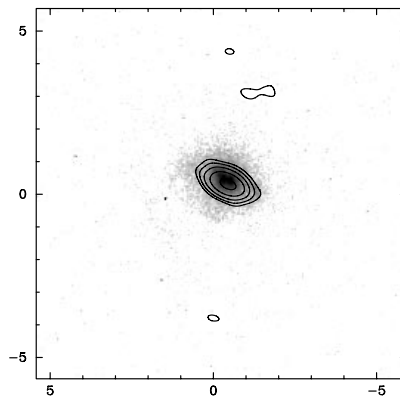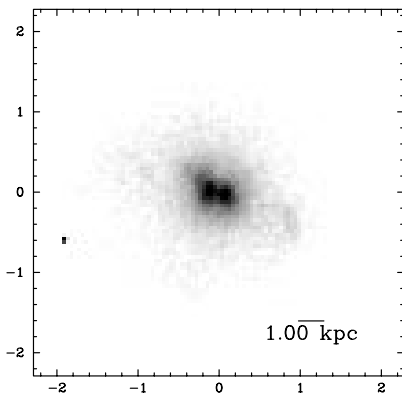
Fig. 21.—3C 284; *left*, original *HST* image; *middle*, *HST* image with radio contours superposed (19); *right*, large-scale radio map (12)
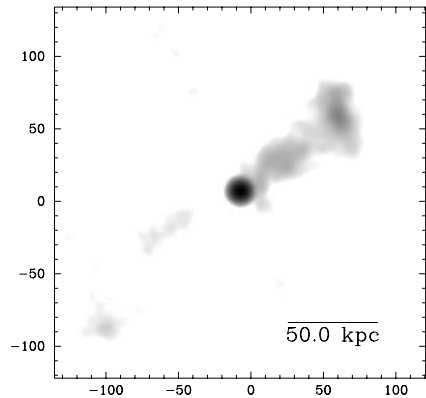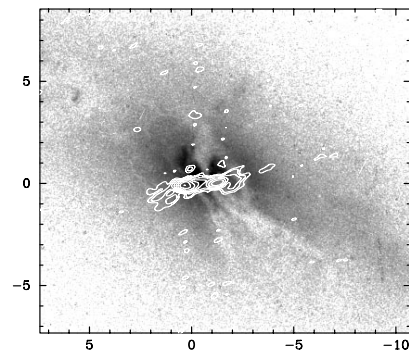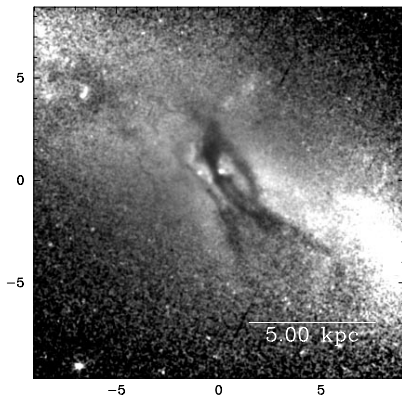
Fig. 22.—3C 293; *left*, absorption map; *middle*, *HST* image with radio contours superposed (19); *right*, large-scale radio map (11)

42
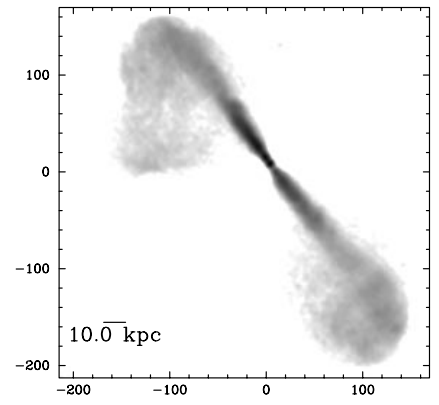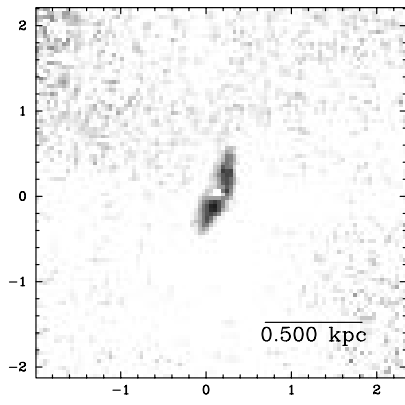
F<small>IG</small>. 23.—3C 296; *left*, absorption map; *right*, large-scale radio map (7)
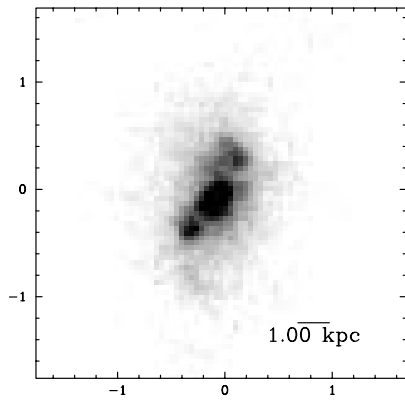
F<small>IG</small>. 24.—3C 303.1; Original *HST* image
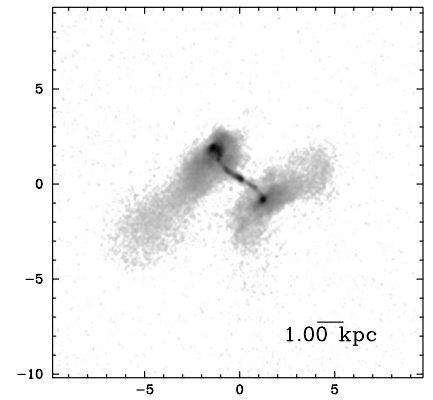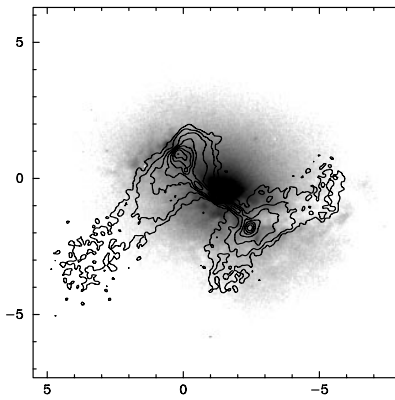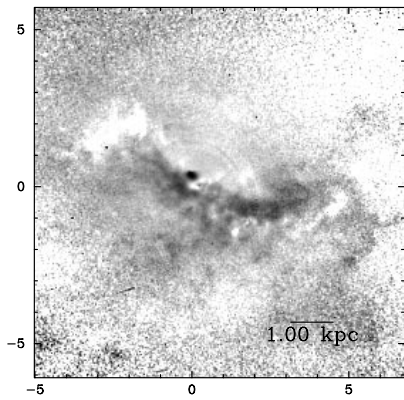
F<small>IG</small>. 25.—3C 305; *left*, absorption map; *middle*, *HST* image with radio contours superposed (13); *right*, large-scale radio map (13)
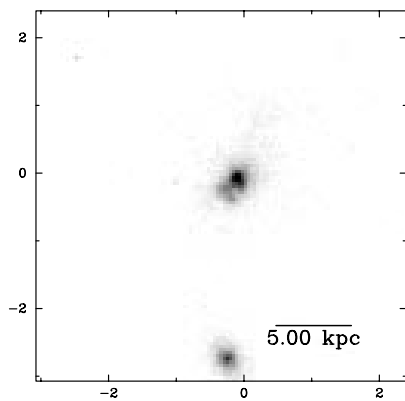
F<small>IG</small>. 26.—3C 306.1; Original *HST* image
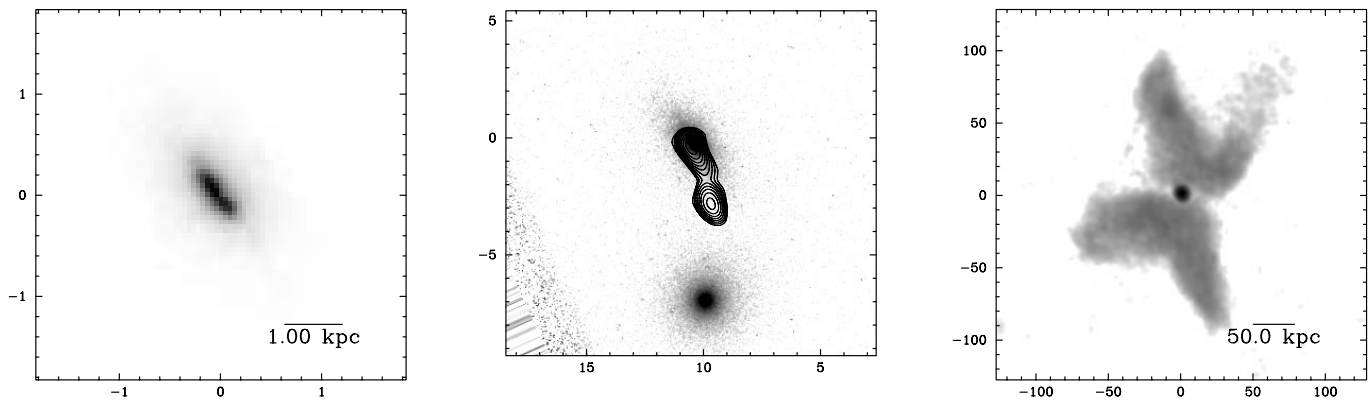
FIG. 27.—3C 315; *left*, original *HST* image; *middle*, *HST* image with radio contours superposed (19); *right*, large-scale radio map (11)
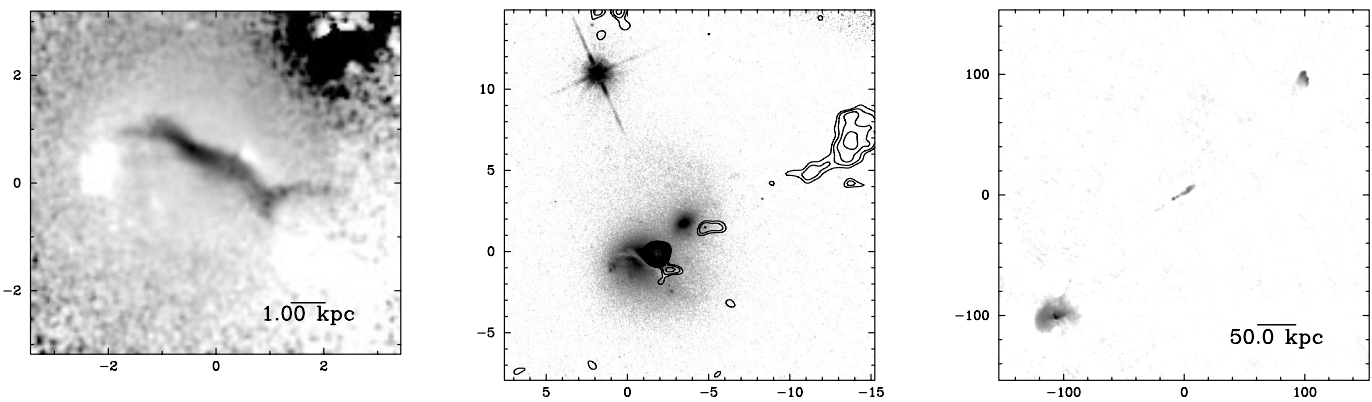
FIG. 28.—3C 321; *left*, absorption map; *middle*, *HST* image with radio contours superposed (19); *right*, large-scale radio map (14)

FIG. 29.—3C 326; *left*, absorption map; *right*, large-scale radio map (2)

FIG. 30.—3C 327; *left*, absorption map; *right*, large-scale radio map (19)

44
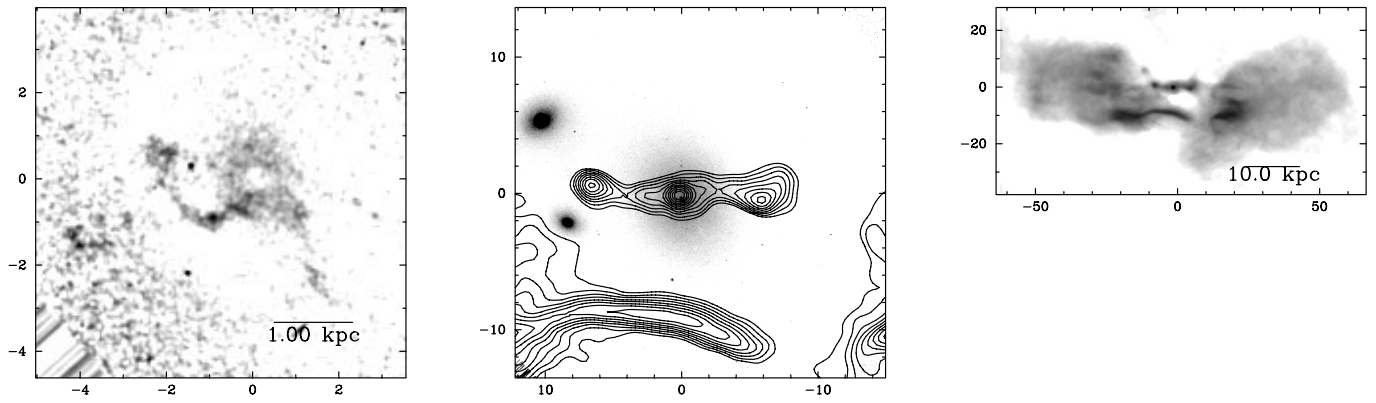
FIG. 31.—3C 338; *left*, absorption map; *middle*, *HST* image with radio contours superposed (15); *right*, large-scale radio map (15)
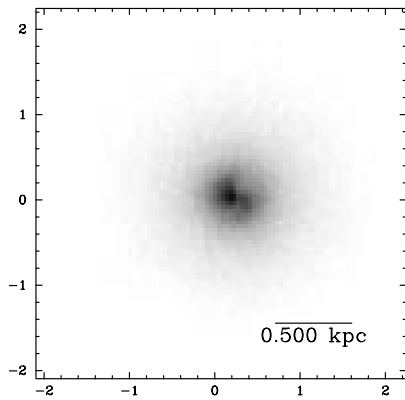
FIG. 32.—3C 353; Original *HST* image
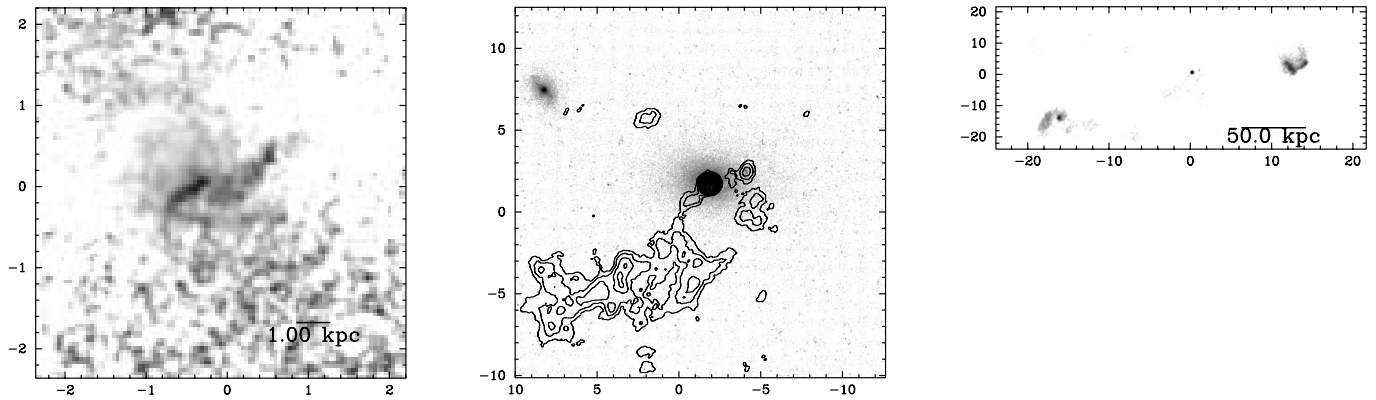
FIG. 33.—3C 357; *left*, absorption map; *middle*, *HST* image with radio contours superposed (19); *right*, large-scale radio map (19)
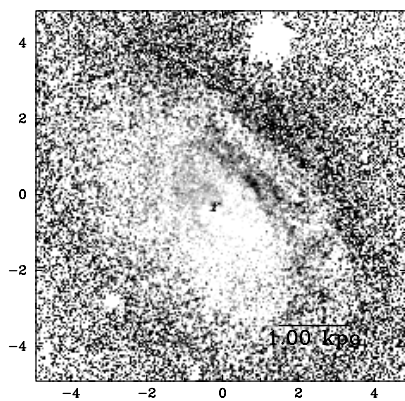
FIG. 34.—3C 403; Absorption map
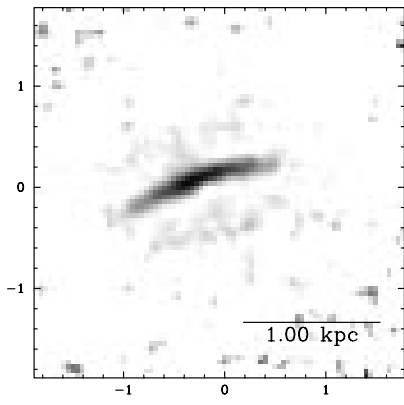
FIG. 35.—3C 430; Absorption map
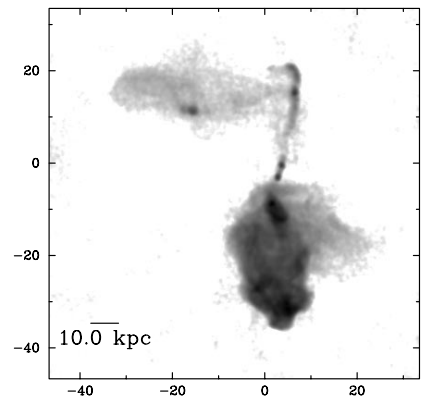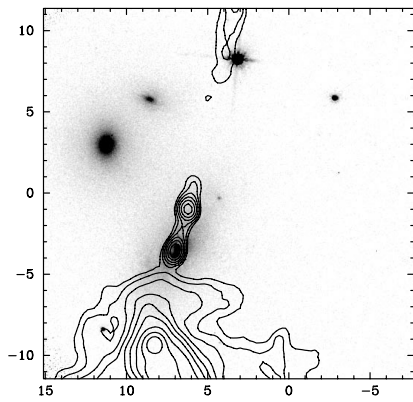
FIG. 36.—3C 433; *left*, absorption map; *middle*, *HST* image with radio contours superposed (16); *right*, large-scale radio map (16)
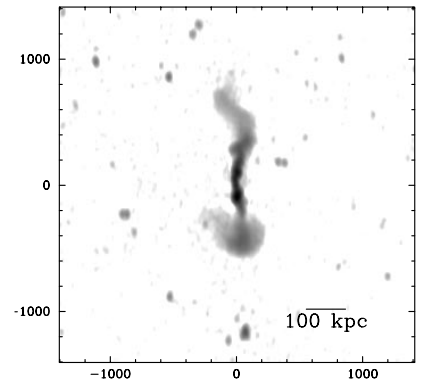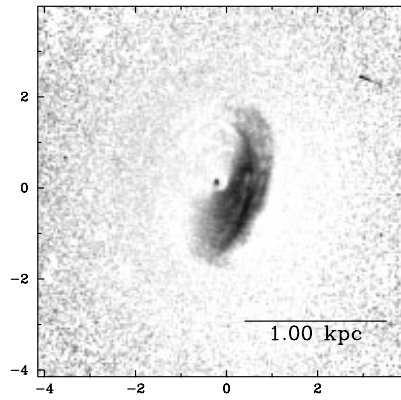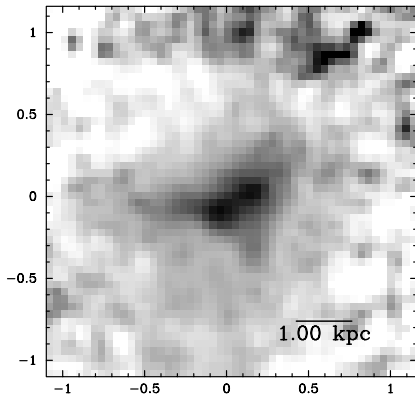
FIG. 37.—3C 436; *left*, absorption map; *middle*, *HST* image with radio contours superposed (17); *right*, large-scale radio map (17)
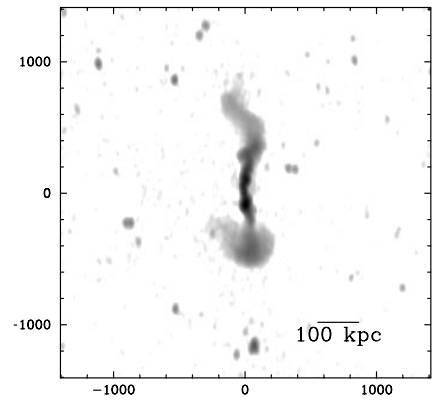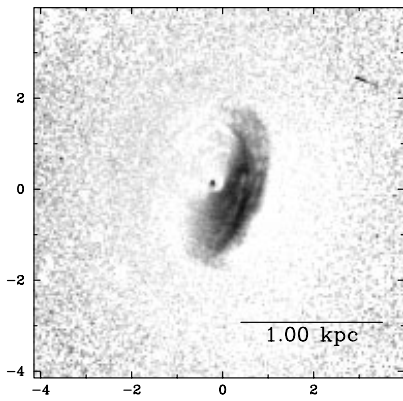
FIG. 38.—3C 449; *left*, absorption map; *right*, large-scale radio map (2)

22) shows multiple dust lanes. At least four different strands of dust twirl around a double or triple galaxy nucleus. The dust exists on a large linear scale (~ 10 kpc). Van Breugel et al. (1984) suggest that the host galaxy of this radio source contains a rotating disk out to a radius of 9 kpc, with a vigorous interaction between twin radio jets and the gas in the disk giving rise to intense small-scale radio emission. On larger scales the radio source shows a weak double-lobed structure, whose orientation is approximately perpendicular to the dust features.

3C 296 (NGC 5532), z = 0.0237.—The absorption map (Fig. 23) shows a sharp, well defined edge-on disk, similar in shape to the one seen in 3C 270, only on a smaller linear scale. The radio map shows a double-sided jet that remains straight over the full size of the source. The lobes are more extended toward the southeast of the jet axis.

3C 303.1, z = 0.267.—The galaxy has an elongated nucleus, the complicated structure of which prevented a model absorption map from being made. Two dark lanes either side of the nucleus are likely to be associated with
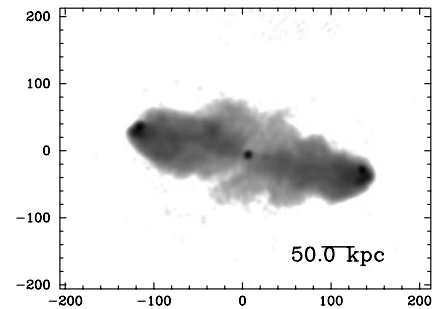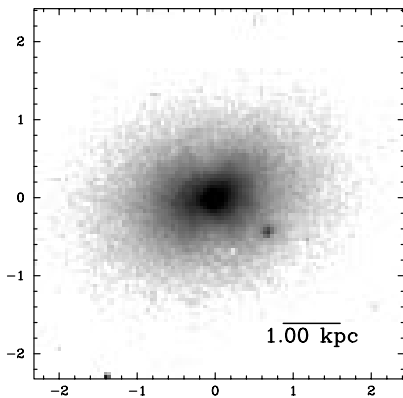
FIG. 39.—3C 452; *left*, original *HST* image; *right*, large-scale radio map (1)
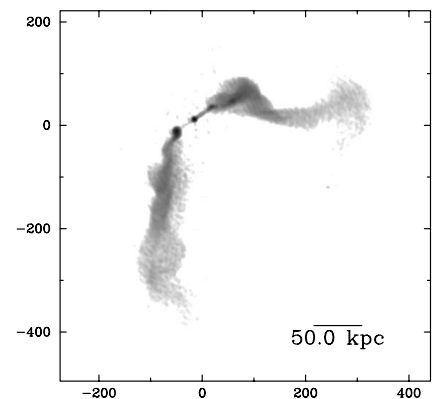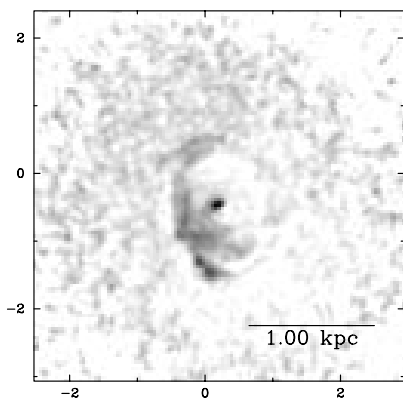
FIG. 40.—3C 465; *left*, absorption map; *right*, large-scale radio map (18)

dust obscuration (Fig. 24). The extended radio source is an asymmetric double $\sim 1\rlap{.}''8$ in size, elongated perpendicular to the two proposed dust lanes.

3C 305, $z = 0.041$.—The absorption map (Fig. 25) shows a bent, S-shaped dust lane with lots of fine structure. There are some extended dust structures in addition to a main dust lane. One of them is in the southeast direction, ending in a diffuse blob of dust. At the west side of the dust lane there is another structure extending to the south, also ending in a diffuse dust structure. Some patches of emission are seen at the end of the main dust lane.

Figure 25 shows a H-shaped radio source. A radio core and two hot spots are seen aligned roughly parallel to the outer dust lane. There is faint radio emission extending to the northwest and southeast. The dust roughly traces the radio emission. This is an example where the radio source and dust are morphologically similar. This source has an extended emission line region of roughly the same dimensions as the radio lobes (Heckman et al. 1982). Jackson et al. (1995) give a review of previous work done on this particular radio galaxy. 3C 305 shows many similarities in its properties to 3C 293.

We note that we find a position angle difference of $\Delta = 19°$ for this object, while Kotanyi & Ekers (1979) find a position angle difference of $\Delta = 117°$. This is due to the different angular resolutions used for the different observations.

3C 306.1, $z = 0.441$.—There are indications of dust absorption southeast of the nucleus (Fig. 26). There is a close (distance ~ 11 kpc) companion that is most likely responsible for the tails of emission that are seen. There may also be a second nucleus. The radio source is a symmetric double (Xu et al. 1995).

3C 315, $z = 0.1083$.—This galaxy has a very flattened shape (Fig. 27) which prohibited the fitting of elliptical isophotes. Part of the nucleus shows clear signs of obscuration by dust. The large-scale radio source is X-shaped, with the central radio emission elongated in the direction perpendicular to the dust. A faint lobe on the west side bends to the north. There is no obvious connection between the optical morphology (which is elongated in the direction of the radio source major axis) and the radio source on large scale.

3C 321, $z = 0.096$.—The absorption map (Fig. 28) shows a disturbed dust lane with some patches of emission at both far ends of the lane. At the east the dust seems to divide itself up into three separate lanes. The galaxy has a close companion to the northwest (distance ~ 5 kpc). The radio source shows a radio jet of length $10''$. On larger scales, two hotspots are seen, at a position angle differing by just over $10°$ from that of the radio jet.

3C 326, $z = 0.0895$.—The absorption map (Fig. 29) shows a sharp, well defined, edge-on disk. East of the nucleus a small dust feature extends from the dust disk to the north. The large-scale, asymmetric radio structure extends roughly in the east-west direction, far from perpendicular to the dust disk.

3C 327, $z = 0.1039$.—Fig. 30 shows a double dust disk northwest of the galaxy nucleus. The galaxy nucleus may be double. There is an indication of two elongated structures of emission emerging from the nucleus. A diffraction spike caused by a nearby star is visible on the image. The large-scale radio map shows a radio core, jet, and two hot spots on one line in roughly an east-west direction.

3C 338 (*NGC 6166*), $z = 0.0298$.—This galaxy lies in the cluster Abell 2199. The absorption map (Fig. 31) shows filamentary dust structures. One arm of dust south of the nucleus has an S shape. Northeast of the nucleus there is a second arm of dust. Some patches of dust are also seen.

Figure 31 shows the central radio contours overlaid on the optical image. Ge & Owen (1994) describe this unusually looking radio source in detail. The optical component northeast of the radio core is related to a weak radio component. 3C 338 was the first radio source in which a two-sided jet was observed on parsec scales. South of the radio core a part of the strange "ridge" first reported by Burns, Schwendeman, & White (1983) is seen. There seems to be no morphological relation between the dust arms and the radio source.

3C 353, $z = 0.0304$.—The original image (Fig. 32) shows an indication of a small dust lane near the nucleus of the galaxy. The large-scale radio structure (Morganti, Killeen, & Tadhunter 1993) is elongated perpendicular to the dust lane.

3C 357, $z = 0.1664$.—In Figure 33 we see a slightly disturbed dust lane that seems to be divided up into two separate lanes. One is located closer to the nucleus and is small in scale. The other lane extends from the nucleus out to the northwest and at the end of the lane there is a patch of emission. A radio emission knot to the west of the nucleus coincides with the optical patch of emission at the end of the dust lane. Thus, this patch of optical emission may be optical synchrotron emission.

3C 403, $z = 0.059$.—There are spiral arms or rings of dust around this galaxy nucleus (Fig. 34). There are two clear arms of dust near the nucleus, and a fainter one further out to the northwest. The radio source is elongated in the east-west direction, with a faint X shape extending to the northwest and southeast (Black et al. 1992), roughly perpendicular to the dust lane.

3C 430, $z = 0.0541$.—Figure 35 shows a sharp, well defined, edge-on disk. The large-scale radio source (Leahy & Williams 1984) shows two prominent bright hot spots at a position angle of $35°$.

3C 433, $z = 0.1016$.—This absorption map (Fig. 36) shows patchy dust features. Patches of dust trail the direction of the radio jet. The radio source is oriented north-south, with the northern arm having a peculiar morphology.

3C 436, $z = 0.2145$.—This absorption map (Fig. 37) indicates a dust lane obscuring part of the galaxy nucleus.

3C 449, $z = 0.0171$.—Figure 38 shows a beautiful dust torus in which considerable detail can be delineated. Distinct arms of dust in the torus can be distinguished, separated by a projected distance of ≈ 55 pc. The radio emission is elongated in north-south direction, roughly along the dust torus, rather than perpendicular to it. The radio jets show some slight bends on large scales.

3C 452, $z = 0.0811$.—Figure 39 shows the original image of 3C 452. There is a weak indication of a faint dust lane near the nucleus leading to the dumbbell shape. The radio source has a bright core and two lobes all on one line roughly perpendicular to the proposed dust lane.

3C 465 (*NGC 7720*), $z = 0.0293$.—This galaxy is the central brightest galaxy in the cluster Abell 2634. The absorption map (Fig. 40) shows arms of dust around the galaxy nucleus. To the south of the nucleus two arms are clearly visible. The large-scale radio source shows two radio

jets and has a "wide angle tail" morphology. The dust disk is roughly perpendicular to the radio jets.

2.4. Analyses of the Dust Structures

A large range of dust morphologies are observed in these galaxies. Seven sharply defined disks are found, one dusty torus, eight objects which show multiple dust lanes, 21 which show single lanes (two of which are distorted), and three objects that show filaments and patches of dust. The reader is reminded, though, that the model absorption maps will detect only the patchy dust, and not any uniformly distributed dust that is present throughout the galaxy; they will also preferentially detect dust close to the near side of the galaxy where the path length through the absorbed starlight is maximum.

On the assumption that the model absorption maps represent the obscuration of light by clumpy dust these maps can be used to investigate the properties of this clumpy dust. Axial ratios and linear sizes of the dust features were measured at a pixel value of 0.85 in the model absorption maps, i.e., where 15% of the emission is absorbed. The axial ratio of a disk can be used to derive an inclination angle for the dust disk with respect to the line of sight. A covering factor of the dust was derived by summing the solid angle covered by all pixels in the model absorption map that have a value of less than 0.85, and converting this to kpc^2. Mean optical depths of the dust were derived using

$$\tau = -\ln(S/S_0), \tag{1}$$

where S/S_0 is the ratio between the sum of counts in the dust area of the original image and the model galaxy image. Estimates for the mass of the clumpy dust were determined using the relation

$$M_{\mathrm{dust}} = \Sigma \langle A_\lambda \rangle \Gamma_\lambda^{-1}, \tag{2}$$

where Σ is the area covered by the dust feature, $\langle A_\lambda \rangle$ is the mean absorption in the dust area, and Γ_λ is the mass absorption coefficient (Sadler & Gerhard 1985). Following van Dokkum & Franx (1995), we adopt the galactic value of the mass absorption coefficient in V band;

$$\Gamma_V \approx 6 \times 10^{-6} \text{ mag kpc}^2 \ M_\odot^{-1}.$$

According to Goudfrooij (1994b), the differences between the extinction curves of elliptical galaxies and the Milky Way are generally small. The parameterized relation from Howarth (1983) for wavelength dependence of the dust extinction from the Milky Way was therefore used to correct for redshift effects.

The masses derived for clumpy dust seen in absorption can be compared to mass estimates of the cool dust in emission as derived from *IRAS* (60 μm) flux densities in the literature (Golombek, Miley, & Neugebauer 1988). Estimates of the cool dust mass (or upper limits thereon if only upper limits to the *IRAS* flux densities are available) can be obtained from the relationship:

$$M_d = \frac{1}{(1+z)} \frac{D^2 S_v}{\kappa_v B_v(T_d)}, \tag{3}$$

where D is the luminosity distance to the source, S_v is the observed flux density, $B_v(T_d)$ is the Planck function for temperature T_d at the rest-frame emission frequency v, and κ_v is the dust opacity.

To derive dust masses some assumptions have to be made for the dust parameters. Adopting a grain size of $a = 0.1$ μm and the value for the grain emissivity factor given by Hildebrand (1983) equation (3) becomes

$$M_d = 5.1 \times 10^{-11} S_v D_{\mathrm{Mpc}}^2 \lambda_\mu^4$$
$$\times [\exp(1.44 \times 10^4/\lambda_\mu T_d) - 1]$$
$$\times (1+z)^{-1} M_\odot. \tag{4}$$

We assumed a dust temperature of $T_d = 30$ K; the logarithm of the derived dust masses are given in Table 2. The dust mass derived with *IRAS* data is expected to give higher values than that of the *HST* absorption maps, since *IRAS* will also detect the uniformly distributed dust. The *IRAS* mass is very sensitive to assumed parameters such as grain size and temperature. As an example, the derived dust masses are a factor of 25 lower if a dust temperature of 50 K is used instead of 30 K. Unshielded, warmer dust particles observed by *IRAS* will therefore cause the derived dust mass to be over estimated.

Figure 41 shows the ratio of the dust mass derived using *IRAS* data to that of the clumpy dust seen in absorption, plotted against the clumpy dust masses. The filled circles represent FR II radio galaxies and the open circles FR I radio galaxies. It is clear that there is a broad range in the fraction of dust in clumps for both FR I and FR II radio galaxies. The dust mass derived using *IRAS* can be higher than the measured clumpy dust mass by a factor of a few to a factor of nearly 1000 (although these factors would be significantly lower if a higher dust temperature were assumed). Further, two-thirds of our sample of radio galaxies have no detected dust absorption features, whilst *IRAS* detections of some of these imply that they do contain dust. Therefore, it is clear that the dust detected in clumpy structures does not correspond to all of the dust in the galaxies and may represent only a small (but variable) proportion.

2.5. Redshift-dependent Selection Effects

The sample spans a redshift range of $0 < z < 0.5$, and determining the presence of dust using morphological signatures becomes more difficult with increasing redshift. Decreasing linear resolution (from ~ 6 pc for the nearest radio galaxy to ~ 500 pc for a radio galaxy at $z = 0.5$) and the loss of signal-to-noise [source brightness $\propto (1+z)^{-4}$] with increasing redshift make detailed dust structures more difficult to delineate. As redshift increases we will preferentially detect the edge-on dust disks, with face-on disks and the extended low surface brightness dust features possibly being missed. At the highest redshifts only the effect of global obscuration of light toward the nucleus is observable.

The observed sizes of the dust features (and the dust spatial coverage) will therefore, on average, be smaller for the higher redshifts, and some dust features will remain undetected in the higher redshift objects. To quantify the extent of this effect, we convolved the images of all radio galaxies with Gaussian functions to simulate the *HST* spatial resolution they would have had if they were located at $z = 0.5$. We further corrected for the decreasing surface brightness by multiplying the signal with $(1 + z)^{-4}$. As an illustration, if 3C 272.1 ($z = 0.0031$, Fig. 18), which shows

TABLE 2

DUST IN RADIO GALAXIES, DUST PROPERTIES

3CR (1)	P.A. (deg) (2)	Δ (deg) (3)	LS (kpc) (4)	b/a (5)	Morphology (6)	Number of lanes (7)	D_{lanes} (kpc) (8)	$\log_{10}$ $(M_d/M_\odot)$ (9)	$\log_{10}$ $(M_{d,I}/M_\odot)$ (10)
3C 20.	0	79.	1.0		Lane (1)	1		4.8	
3C 31.			2.5	0.75	Face-on disk, spiral (1)	>5	0.7	5.3	6.6
3C 46.	145	77.	1.3		Lane (1)	1		5.1	
3C 52.	148	46.	2.0		Lane (1)	1		5.1	
3C 83.1	171	85.	0.8	0.09	Edge on disk (1)	1			6.3
3C 84.			17.0		Extended, complex (2)			5.6	7.8
3C 88.	136	80.	1.0		Faint lane (1)	1		4.2	6.7
3C 136.1	89	17.	0.3		Lane + faint structure (1)	1			
3C 171.	173	73.	0.5		Lane (1)	1			7.7
3C 173.1	99	82.	0.8		Lane (1)	1		4.9	<8.1
3C 180.	90	83	1.4		Lane (1)	1			
3C 196.1	143	84.	0.6		Lane (double?) (1)	2?	0.7		
3C 223.1	40	56.	10.0	0.33	Double lane (1)	2	0.9	6.2	
3C 236.	174	57.	10.0	0.45	Mult. lane (1)	2	1.1	6.5	7.3
3C 264.			0.5	1.	Face-on disk/optical jet (1)	1		4.5	<6.3
3C 268.2	81	60.	1.0		Lane (1)	1			
3C 270.	170	84.	0.3	0.42	Disk (1)	1		3.0	<5.4
3C 272.1	81	85.	1.3	0.3	Multiple lanes (1)	3	0.08	3.6	5.2
3C 274.1	7	49.	1.6		Lane (1)	1			
3C 275.	126	75.	1.0		Lane (1)	1			
3C 284.	0	87.	1.2		Lane (1)	1			8.2
3C 293.	22	70.	10.0		Complex system, 5 lanes (2)	5	0.5	6.3	7.1
3C 296.	160	57.	0.5	0.29	Disk (1)	1		3.6	<6.4
3C 303.1	49	83.	0.8		Lane (1)	1			8.2
3C 305.	64	19.	7.0	0.43	Warped lane, patches (2)	1		6.2	7.2
3C 306.1	45	45.	2.0		Lane + faint structure (1)	1		6.1	
3C 315.	120	85.	0.3		Lane (1)	1		5.1	<7.2
3C 321.	69	51.	10.0	0.17	Distorted lane (2)	1		5.7	8.4
3C 326.	104	23.	4.2	0.24	Disk (1)	1		5.4	
3C 327.	36	64.	5.0	0.30	Multiple lanes, patches (2)	2	0.6	5.9	8.3
3C 338.	158	69.	2.8		One-sided filaments (2)	2	...	5.1	<6.4
3C 353.	166	82.	0.3		Faint lane (1)	1		3.3	
3C 357.	127	16.	9.0		Multiple lanes (2)	3	0.7	5.8	
3C 403.	48	16.	3.8	0.49	Multiple lanes (2)	3	1.3	6.4	7.6
3C 430.	110	75.	1.5	0.15	Disk (1)	1		4.5	
3C 433.			8.0		Complex, patchy (2)			5.7	7.9
3C 436.	74	73	2.5	0.25	Lane (1)	1		5.9	<7.9
3C 449.	169	19.	1.3	0.50	Torus (1)	5	0.09	4.5	6.0
3C 452.	14	66.	2.3	0.27	Faint lane (1)	1		5.1	
3C 465.	8	66.	1.1	0.69	Lane (1)	2	0.2	4.0	6.6

NOTES.—Col. (2), position angle of dust feature in degrees, measured north through east, as close to the nucleus as possible; col. (3), position angle difference between the dust feature and the radio source in degrees; col. (4), largest linear size of the dust feature in kiloparsec; col. (5), axial ratio of the dust feature; col. (6), description of the dust morphology; in parentheses the classification, as defined in § 3.1; col. (7), number of lanes/arms in the dust; col. (8), projected distance (in kpc) between the two most prominent arms/lanes of dust; col. (9), logarithm of the derived dust mass in $M_\odot$, from the absorption maps; col. (10), logarithm of the derived dust mass in $M_\odot$, from the *IRAS* data.

multiple dust lanes in great detail, were observed at a redshift of 0.5, then the isophotes would be slightly disturbed but it would not reach the dust detection limit. If 3C 338 ($z = 0.0298$, Fig. 31), which shows a strand of dust on one side of the galaxy nucleus, were observed at $z = 0.5$, we would distinguish a small disturbance in the isophotes on the side of the dust filament and we would classify it as having nuclear dust. The appearance of the galaxies observed at higher redshifts are in fact similar to the appearance of the convolved images of the nearby dusty radio galaxies, increasing our confidence that the isophotical disturbances of the higher redshifts source are due to the presence of dust concentrations.

The linear size of the dust and the dust mass that we would determine if the radio galaxies were at redshift 0.5

were calculated from the convolved images. We find a small mean decrease of the linear size of the dust ($\approx 5\%$ for galaxies at $z = 0.1$), but a much larger decrease in the dust masses (see Fig. 42). The dust mass changes for most lower redshift radio galaxies, with much scatter in the size of the change being introduced by the different morphologies of the dust at low redshifts. Smaller clumps of dust within nearby radio galaxies would not be detected at higher redshifts, and indeed dust would not be detected at all at $z = 0.5$ for 3C 88, 3C 270, 3C 272.1, and 3C 315.

To maximize accuracy we have used the values for all parameters derived using the unconvolved images: use of the convolved dust masses would only serve to strengthen some of the conclusions drawn in this paper. Still, because this sample covers a relatively wide range in redshift and
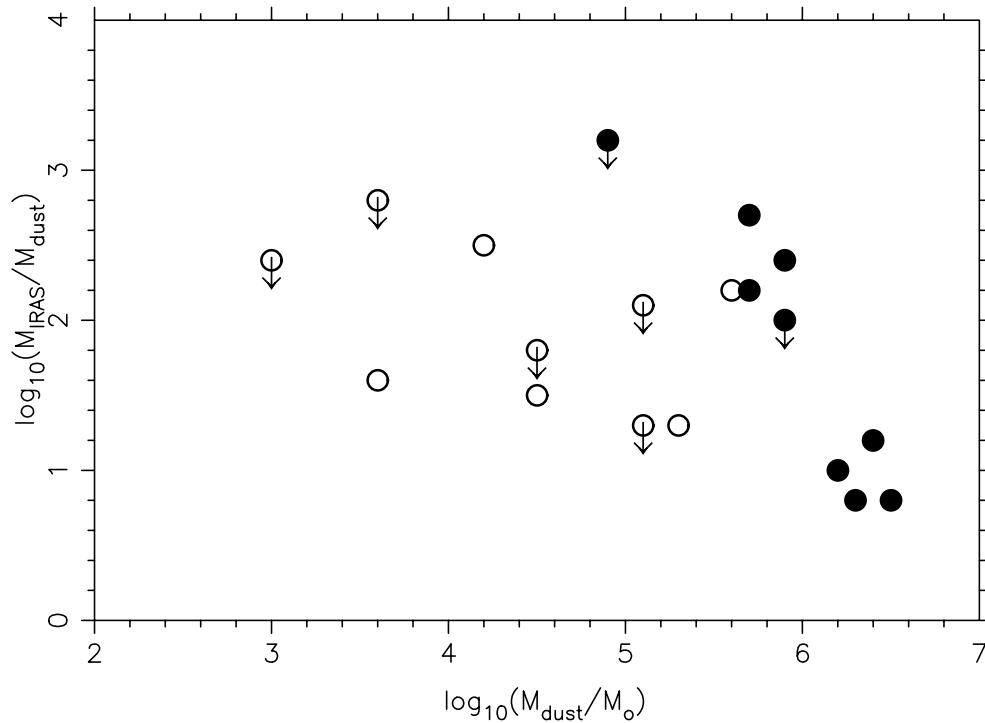
FIG. 41.—Ratio of the dust mass derived using *IRAS* data to the dust mass derived using the residual maps, vs. the dust mass derived using the residual maps. The filled circles represent the FR II radio galaxies that have clumpy dust; the open circles are FR I radio galaxies that have clumpy dust.

because of the assumptions we made for deriving dust properties from the model absorption maps, we must be cautious in our interpretations of the quantitative parameters derived from these data. Correlations found with redshift-dependent quantities (e.g., radio power) may be due to selection effects. However, conclusions based on mor-

phological parameters (e.g., position angles of the dust) are more firmly based.

3. RESULTS

In the coming section we concentrate on the structures of the clumpy dust in the 40 radio galaxies in which it is
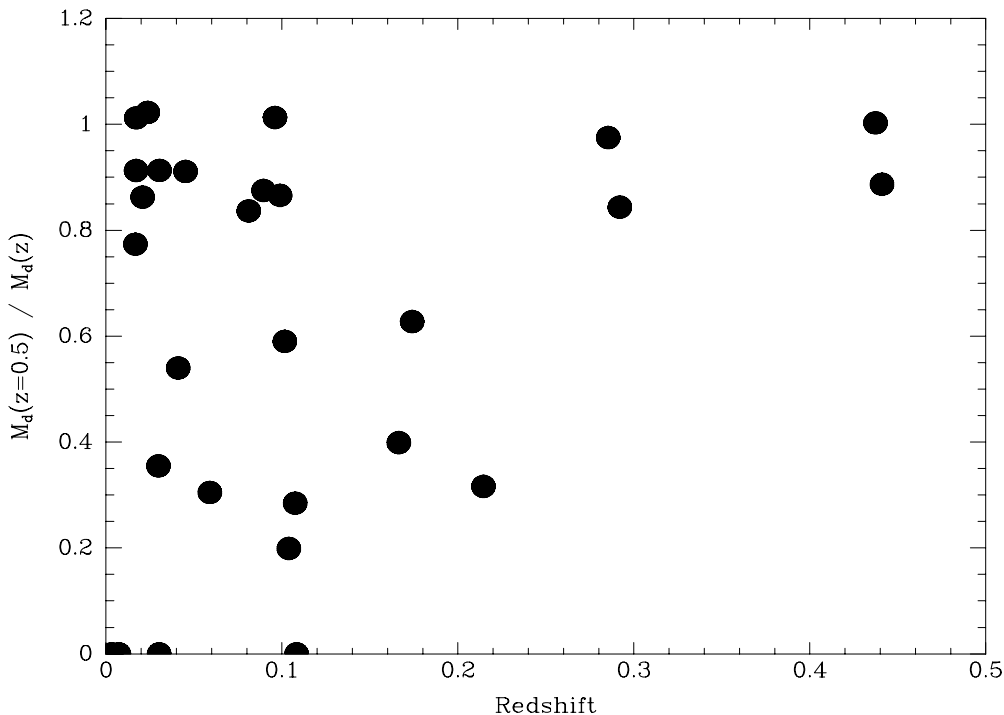
FIG. 42.—Logarithm of the ratio of dust mass derived at $z = 0.5$ to dust mass at z, vs. redshift. For four galaxies the dust could not be detected if the source were to be observed at a redshift of 0.5. The two cases with values fractionally above one, implying that more dust would be detected at higher redshift, occur because with the larger physical pixels at higher redshift, fractionally more dust happened to fall in pixels above the detection limit.

observed. We return to discuss the properties of the sample as a whole in § 4.

3.1. *Dust Morphologies*

The "model absorption maps" of the dusty radio galaxies show a great range in dust morphology. We see settled structures (disks, lanes) and structures that do not appear to be in equilibrium (filaments, patches, lanes with sudden twists). Table 2 lists the morphologies according to five categories: disks, lanes, multiple lanes, patches, and filaments. It is instructive to divide the sample into two morphological groups. The first group comprises the dust disks, lanes, and multiple lanes, and the second group the patchy dust, filaments, and warped and complex multiple lanes (e.g., 3C 293). The two groups can be regarded as representing different dynamical states of the dust. In group one the clumpy dust seems to have settled into an orbit around the galaxy nucleus, while for group two it is still settling. The result of the analyses are summarized in Table 2. A morphological description of the dust is given, together with the number of lanes/arms. The projected distance between the most prominent arms is also given.

10 out of 12 FR I radio galaxies have their clumpy dust in settled states. Only 3C 84 (Fig. 6) and 3C 338 (Fig. 31) show dust that is not settled in a disk or lane, the latter also showing a very peculiar radio structure. For the FR II radio galaxies, we find a range of clumpy dust morphologies, from settled to filamentary.

3.2. *Dust-Radio Orientations*

Kotanyi & Ekers (1979) found that for their sample of seven radio galaxies the major axis of the dust lanes are perpendicular to the radio source axis. It is interesting to investigate this correlation between dust and radio source using higher resolution data which provide information closer to the nucleus where the interaction is likely to be more important.

To investigate relationships between the radio source and dust morphologies we measured the position angle difference between the radio source and the dust features for each object that shows clumpy dust. The position angles of the dust features were measured from north through east at a distance from the galaxy nucleus of 1 kpc or less, except for four cases where it was impossible to measure the position angle of a dust feature because the dust was distributed in a filamentary fashion throughout the entire galaxy (3C 84 and 3C 433), or we viewed the dust disk face-on (3C 31 and 3C 264). The position angle of the radio source was obtained from radio maps obtained in the VLA snapshot survey or available in the literature. Where possible, this was measured from the position angle of the radio jet close to the nucleus, since this gives the best measure of the position angle difference between the dust disk and the axis of the radio source. In sources for which no radio jets were detected, the position angle of the hotspots or large-scale radio structure was used instead; for sources that show both jets and hotspots there is typically less than 10° difference between their position angles. The important properties of the radio data are summarized in Table 1.

Figure 43 shows the distribution of the measured position angle differences between the dust and radio structures of these galaxies, excluding the four sources (three FR I's and one FR II) for which this angle could not be measured, as discussed above (these sources are similarly excluded
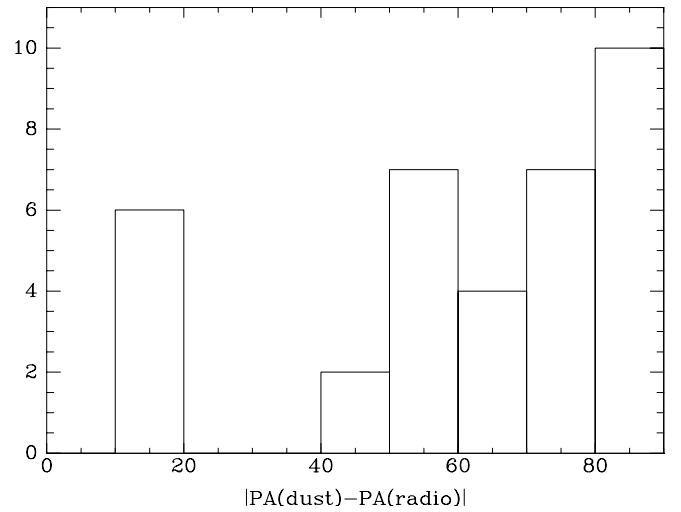
FIG. 43.—Distribution of the position angle difference between the radio source and the clumpy dust feature for the full sample.

from Figures 44, 45, 46, and 47). There is a tendency for the radio source axis to be perpendicular to the dust lanes, although we find a dispersion in the result. The distribution of observed position angle differences, Δ, shows a peak toward 90° and a tail extending out to a position angle difference of 16°. However, the *observed* position angle difference between the dust disk and the radio jet, Δ, will change with the *orientation* of the system with respect to the observer. The observed and real position angle difference
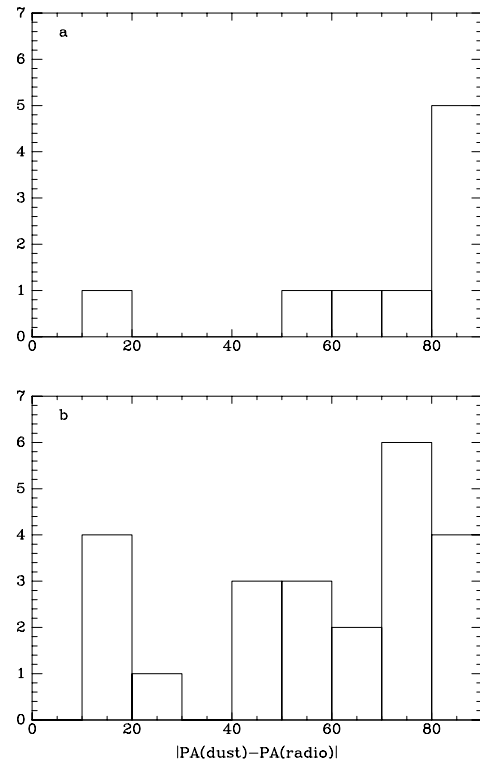
FIG. 44.—Distributions of the position angle difference between the dust feature and the radio source for (*a*) FR I and (*b*) FR II radio galaxies.
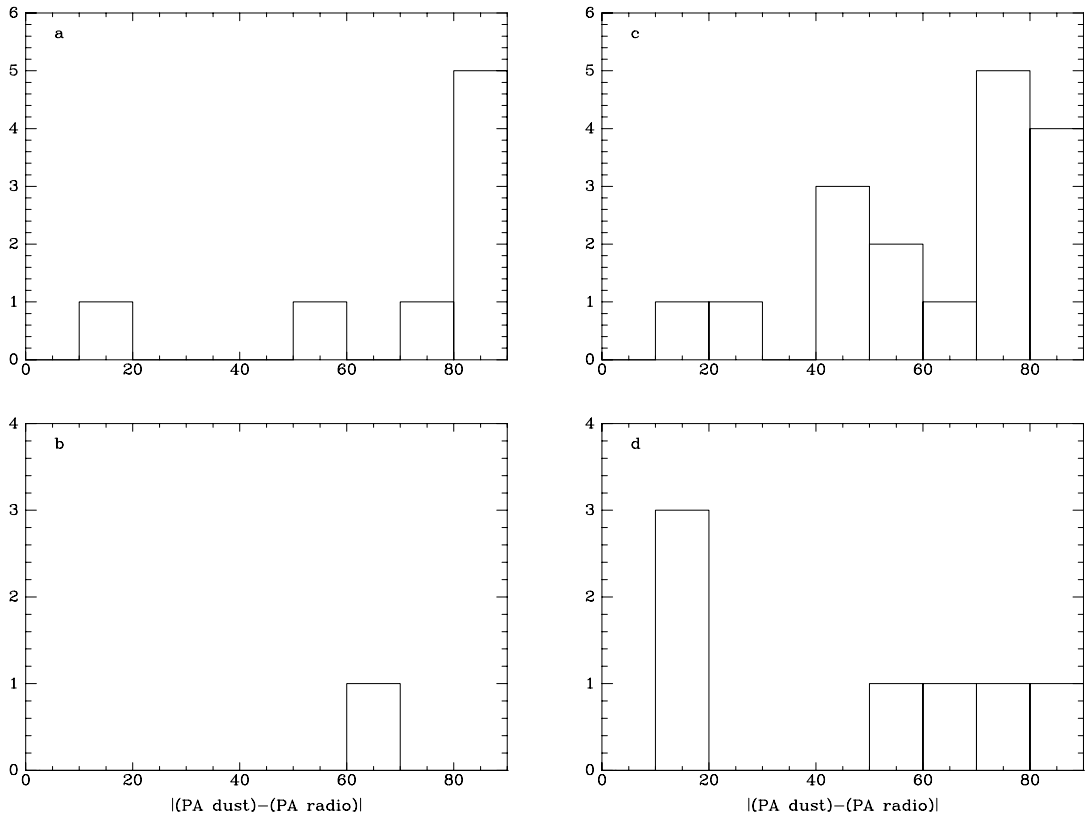
FIG. 45.—Distribution of the position angle difference for different dust morphologies, and FR types. (*a*) FR I with dust in a disk, (*b*) FR I with dust not in a disk, (*c*) FR II with dust in a disk, (*d*) FR II with dust not in a disk.
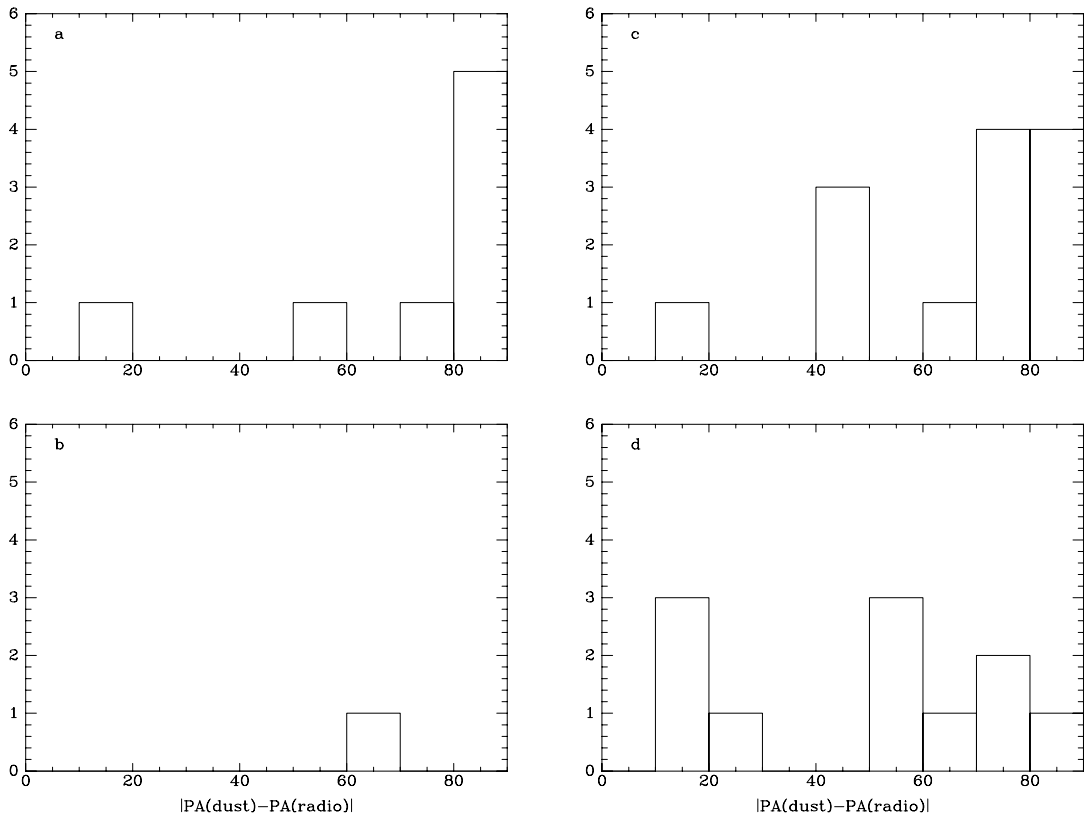
FIG. 46.—Distribution of the position angle difference for different dust sizes, and FR types. (*a*) FR I with dust size less than 2.5 kpc, (*b*) FR I with dust size greater than 2.5 kpc, (*c*) FR II with dust size less than 2.5 kpc, (*d*) FR II with dust size greater than 2.5 kpc.
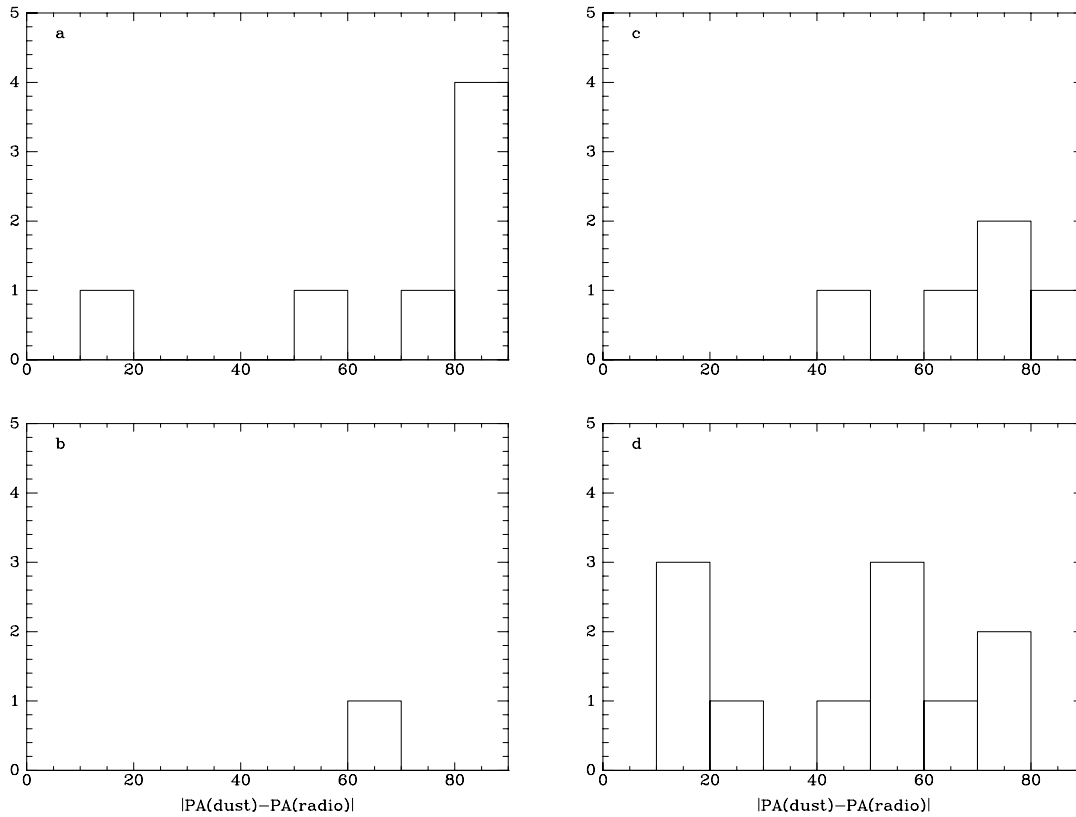
FIG. 47.—Distributions of the position angle difference for different dust masses, and FR types. (a) FR I with log (M_d) < 5.2, (b) FR I with log (M_d) > 5.2, (c) FR II with log (M_d) < 5.2, (d) FR II with log (M_d) > 5.2.

are related to each other by the following relation:

$$\Delta = \arctan \left[\frac{\cos (i) \sin (\theta) \sin (\phi) + \sin (i) \cos (\phi)}{\cos (\theta) \sin (\phi)} \right], \quad (5)$$

where i is the inclination of the dust disk relative to the line of sight, the angle ϕ is the angle between the radio jet and the normal of the dust plane, and the angle θ gives the direction of the projected radio jet on the plane of the dust disk. The real angle between the plane of the dust and the radio jet Δ_{real} is given by $90° - \phi$.

The observed distribution of Δ can be reproduced using an intrinsic flat distribution of position angles of the radio jet with respect to the dust disk for which $55° \leq \Delta_{real} \leq 90°$, and varying the orientation of the system (i.e., i, θ) randomly. A two-sided KS test shows that the generated distribution and the observed distribution are drawn from the same parent population at a 95% confidence level.

Comparing the orientation of a dust disk (by looking at the axial ratio of the projected dust feature and the side of the disk where most light is absorbed) and the radio source (by looking at the jet-sidedness of the source) supports the result that for the majority of the objects the radio source and dust disk are oriented perpendicular to each other (for example 3C 31, 3C 264, 3C 296, 3C 465). This is not true of all sources, however. In some cases the radio sources appears to have a similar orientation to the dust disk, and to interact directly with it. For 3C 264 we have previously suggested that the radio jet propagates right into the dust disk (Baum et al. 1997). In other examples (e.g., 3C 293) the radio jet is known to interact strongly with the emission line

gas, and our data suggest an association between the gas and the dust. This considered, it may be possible that for the radio galaxies that are represented in the tail of the distribution of Δ, the radio sources are physically interacting with the dust and that for the remainder the position angle difference is biased even more strongly toward perpendicular.

3.3. Correlations with FR Type

3.3.1. Dust-Radio Orientations

Figure 44 shows the distribution of Δ for FR I and FR II radio galaxies separately. There are four galaxies for which the FR type is not known, and these are included in neither sample. It is directly clear that there is a difference between the relation between dust and radio source for FR I and FR II radio galaxies. We find there is a strong tendency for the radio jet to be perpendicular to the dust major axis for FR I radio galaxies. This effect is not so strong for FR IIs. A Kolomogorov-Smirnov test was used to test if the distribution of Δ was consistent with a flat distribution across all position angles: the test was done for FR I and FR II galaxies separately and for the full sample, the results being shown in Table 3. The probabilities will be upper limits because of the low number statistics (especially for the FR I sample).

3.3.2. Dust Properties

We find a correlation between the observed position angle difference Δ and the *morphology* of the dust. Figure 45 shows the distribution of Δ for the two different dust morphology groups, settled and unsettled, as described in § 3.1

TABLE 3

DUST IN RADIO GALAXIES, STATISTICS

Sample (1)	Δ (2)	Δ (1) (3)	Δ (2) (4)	$\Delta\ L_d < 2.5$ (5)	$\Delta\ L_d > 2.5$ (6)	$\Delta\ M_d < 5.2$ (7)	$\Delta\ M_d > 5.2$ (8)
FR I.......	6.8	6.9	...	6.9	...	16.1	...
FR II......	14.4	5.7	69.8	8.3	76.6	63.5	82.7
All	**0.1**	**0.04**	87.9	**0.04**	70.6	**0.3**	82.7

NOTES.—Two-sided Kolmogorov-Smirnov test statistics indicating the probability that the distribution of Δ is a uniform distribution. The tests are done for FR I, FR II, and the full sample separately. Col. (2) gives the probability that the position angle differences are distributed uniformly. In cols. (3) and (4) the sample is divided for (1) disklike dust features and (2) less settled dust features. For cols. (5) and (6) the sample is divided by the size of the dust feature (smaller and larger than 2.5 kpc). The statistics for objects with low dust masses is given in col. (7), and high dust masses in col. (8).

and indicated in Table 2. Again the sample was split according to FR type. It is directly clear that the majority (9 out of 12) of FR I radio galaxies have dust in settled structures (note that three of these are not included on Fig. 45 because their dust position angle could not be measured, as discussed above) and that there is a strong tendency for these structures to be perpendicular to the radio source. For FR II sources, the galaxies that have dust in disks and lanes show a strong preference for the radio jet to be perpendicular to the dust major axis; for the dust structures that show patches or filaments of dust there does not seem to be such a preference, and the dust features are randomly oriented with respect to the radio jet.

A correlation also exists for FR II type radio galaxies between Δ and the *linear size* of the dust feature. Figure 46 shows the distribution of Δ for the sources where size of the dust is smaller than 2.5 kpc, and the sources where the size of the dust is larger than 2.5 kpc. For small-scale dust features the dust major axis and the radio source tend to be perpendicular to each other, while for the radio galaxies that display dust on larger scales there is no preference for the orientation of the dust axis with respect to the radio axis. Only two FR I radio galaxies have dust sizes larger than 2.5 kpc (3C 338 with a dust size of 2.8 kpc and 3C 84 with a dust size of 17 kpc). Note that most dust disks (primarily found in FR I radio galaxies) are small-scale dust features. No correlation is seen between Δ and the dust coverage per square area. Evidently, the measure of how far out the dust reaches from the nucleus of the galaxy is more important than the total covering factor of the dust.

3.3.3. *Dust Masses*

Correlations also exist between Δ and the estimated mass of the dust. From Figure 47 we see that the FR Is have relatively small dust masses. For FR II sources, more galaxies have high dust masses (although at higher redshift we would miss the low-mass dust features) but, for the five that have measured position angles and lower dust masses, the dust is roughly perpendicular to the radio source.

It appears then, that FR I and FR II radio galaxies are significantly different in their (clumpy) dust properties. FR I sources that display clumpy dust typically have a relatively low mass of clumpy dust in a small disk around the nucleus, oriented perpendicular to the radio source. FR II sources that display clumpy dust exhibit a wider range of dust sizes, morphologies, and masses; only those FR II sources with clumpy dust on small scales in disklike structures show a strong preference for the dust to be oriented perpendicular to the radio source.

4. COMPARISON WITH RADIO-QUIET SOURCES

We can compare the estimated masses of clumpy dust in our sample to the estimated dust masses for early-type galaxies as derived by van Dokkum & Franx (1995), also using *HST* data, because they used the same method for deriving dust masses as we do. The dust mass in their paper represents the mass of both dust and gas, for which they use the Galactic gas-to-dust ratio of 130; we convert back by this factor to give the mass of the dust only, which can then be directly compared with the dust masses we measure for the radio-loud sources. 3C 338 (NGC 6166) is part of both our sample and that of van Dokkum & Franx, and so can be used as a control source. We find exactly the same dust mass for NGC 6166 as they do. The van Dokkum & Franx sample includes a number of galaxies that show extended radio emission; for the comparison, we consider only the 19 radio-quiet early-type galaxies in their sample.

Figure 48 shows a plot of the estimated clumpy dust masses of the 3CR sample (*open circles*, FR I; *asterisks*, FR II's) and the early-type galaxies of the van Dokkum & Franx sample (*filled triangles*). Only those galaxies with detected clumpy dust are plotted. As explained in § 2.2, we considered only galaxies in which dust was detected over a minimum area of 3×3 pixels with more than 20% of the light in this area being absorbed, and these criteria do not give a fixed dust mass detection limit since the limit will depend upon the surface brightness of the emission underlying the dust. However, if we assume that the galaxies are intrinsically similar, the surface brightness evolving simply due to cosmological effects as $(1 + z)^{-4}$, then an approximate functional form for the dust mass detection limit as a function of redshift for the 3CR galaxies can be calculated, and it is shown as the solid line on the figure.

The two lower panels in Figure 49 show histograms of the distributions of the clumpy dust masses for FR I and FR II type radio galaxies separately. The logarithms of the dust masses vary between 3.0 and 6.5 $M_{\odot}$, with a mean $\log{(M_d)}_{\mathrm{mean}} = 4.4$ ($\sigma = 0.9$) for FR I radio galaxies, and a mean $\log{(M_d)}_{\mathrm{mean}} = 5.7$ ($\sigma = 0.5$) for FR II radio galaxies. Note that the distributions are quite narrow. The top panel of Figure 49 gives the distribution of dust masses for the van Dokkum & Franx sample of "ordinary ellipticals." The dust masses they find for their sample have a mean $\log{(M_d)}_{\mathrm{mean}} = 3.1$ ($\sigma = 0.9$).

Care needs to be taken when considering the differences between the various samples because of the large number of upper limits not considered, and because of the difference in redshift coverage and consequently signal-to-noise ratios of
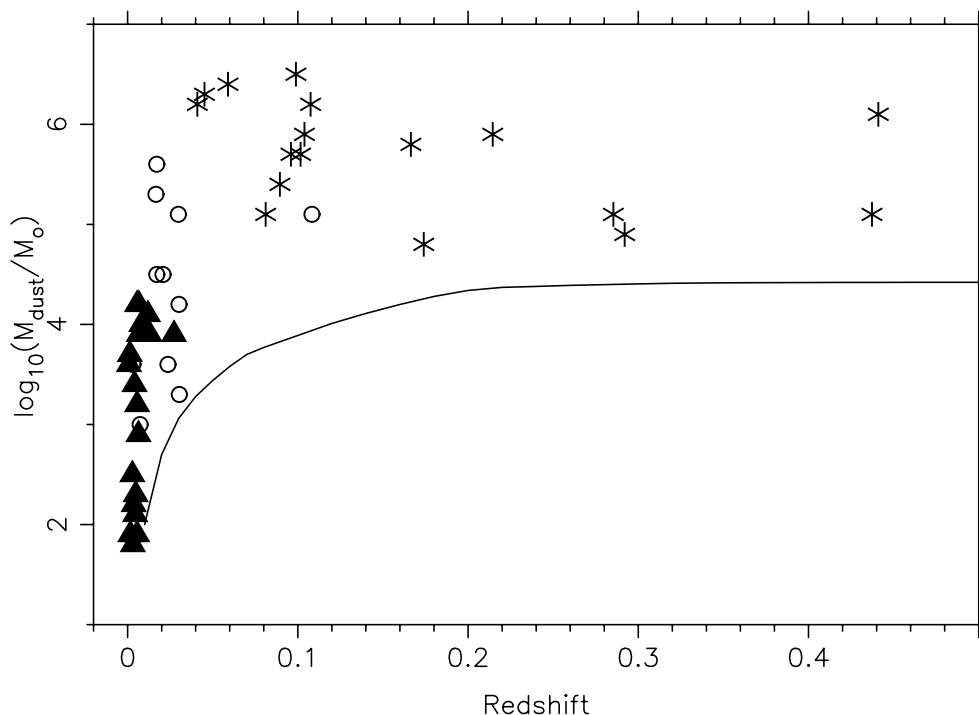
Fig. 48.—Estimated dust masses vs. redshift for three samples of objects. The open circles represent the 3CR FR I galaxies, the asterisks represent the 3CR FR II galaxies, and the filled triangles represent the radio-quiet early-type galaxies from van Dokkum & Franx (1995). The solid line indicates an approximate detection limit for dust masses for the 3CR sample.

the different samples. However, considering only the low z galaxies it is clear that there is a sparsity of both radio-quiet early-type galaxies and FR I galaxies that have high masses of clumpy dust in them. Considering instead the dust masses that would be measured after convolving the images to a redshift of 0.5 would only strengthen this effect. Further, although the FR II's are typically at the higher redshifts prohibiting low clumpy dust masses from being determined, Figure 49 shows that even the lower redshift FR II's tend to have high clumpy dust masses, well above the detection limit, if dust is detected at all in absorption. We conclude, therefore, that high clumpy dust masses are generally found only in radio-loud galaxies, preferentially FR II's.

In order to ensure that the higher dust masses in the radio-loud galaxies are not simply associated with these being more massive galaxies than those in the radio-quiet sample, absolute R-band magnitudes were calculated for all of the galaxies. For the radio-quiet sample the B-band absolute magnitudes of van Dokkum & Franx (1995) were converted to R-band absolute magnitudes taking $B - R \approx 1.3$ and correcting for the different cosmology assumed as compared to the current paper. For the 3CR sources with redshifts $z < 0.1$, the apparent R magnitudes of Martel et al. (1999) were simply converted to absolute R magnitudes, K-corrections (of <0.1 mag) having already been applied by Martel et al. (1999). Absolute magnitudes for the 3CR sources with $0.1 < z < 0.5$ were calculated from the apparent magnitudes presented by de Koff et al. (1996), adopting the K-correction appropriate for an elliptical galaxy in the R-band derived by Poggianti (1997). The resultant values are provided in Table 1.

Figure 50 shows the estimated clumpy dust mass plotted against absolute magnitude for the objects in the three

samples. It is clear from the figure that whilst the radio-loud sources are, on average, slightly more massive than those of the radio-quiet sources, the distribution of absolute magnitudes of the populations span a similar range, and any difference in absolute magnitude is substantially smaller than the observed differences in the dust masses. The difference between the masses of clumpy dust in radio-loud and radio-quiet sources is not due to differences in the absolute magnitude of the galaxies.

We conclude that, for galaxies that display strong absorption features due to dust, the mass and morphology of the clumpy dust is related to the radio activity of the galaxy.

5. DISCUSSION

5.1. The Origin of the Clumpy Dust

Dust can be created through different processes. The main source from inside the galaxy that contributes to the interstellar medium is the shedding of matter by evolved stars. The matter is blown into the intergalactic medium by galactic winds, powered by supernovae energy output. With time, the dust will be bound to the potential well of the massive elliptical galaxy. However, there is evidence that the velocity fields of the gas and the stars in radio-loud (and radio-quiet) ellipticals are not coupled (Goudfrooij 1994a and references therein). This suggests an external origin for the gas and dust.

An elliptical galaxy can undergo a merger with a dust-rich galaxy, or it can acquire dust by tidal stripping during a near encounter with a close neighboring galaxy. This way, when the dust and gas get bound to the potential of the massive elliptical, the velocity field of the gas/dust will be random with respect to the stellar velocity field. Shortly
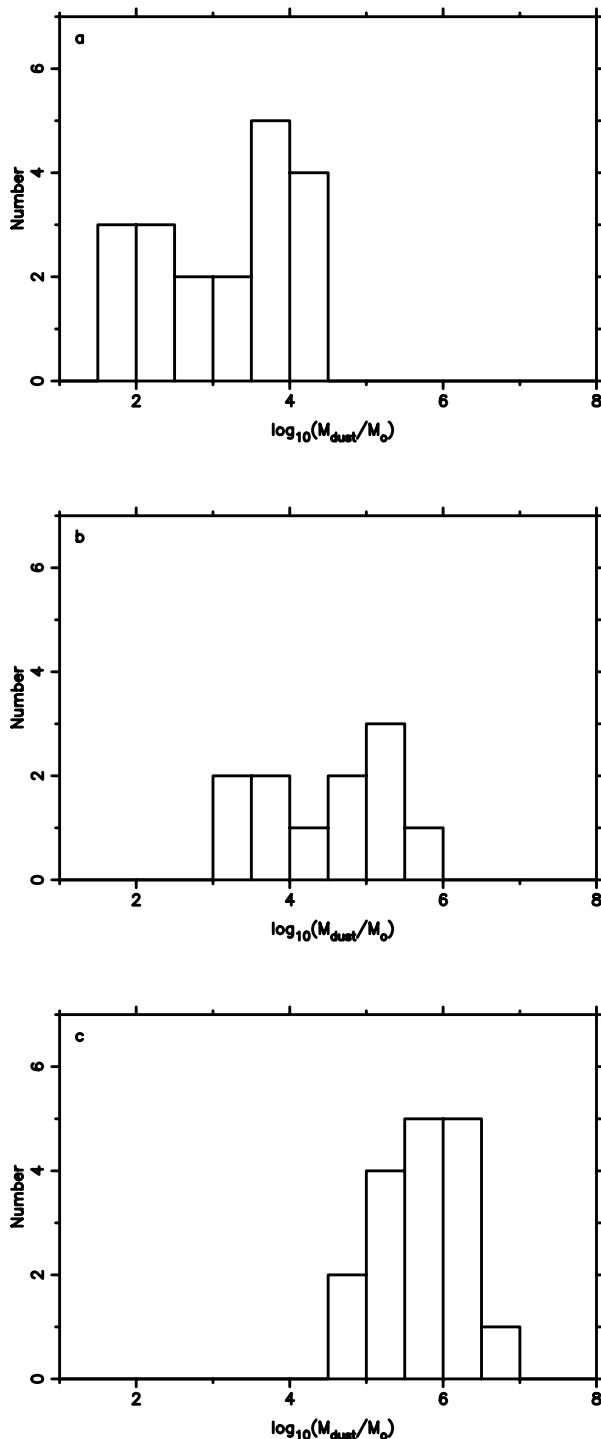
FIG. 49.—Distribution of the logarithm of the dust mass derived using the model absorption maps in $M_{\odot}$. The upper panel (a) shows the distribution for early-type elliptical galaxies that do not show extended radio structure, from van Dokkum & Franx (1995). The lower panels show the distribution for (b) FR I and (c) FR II radio galaxies described in this paper.

after the capture the dust is expected to be distributed throughout the galaxy in a filamentary fashion. With time it will settle into equilibrium orbits around the nucleus. The formation of gaseous disks takes place after a few orbits around the accreting galaxy, i.e., in ~0.5–2 Gyr after capture (Steinman-Cameron 1991). This implies that the

origin of the dust is closely related to the evolutionary history of the parent galaxy and that by examining the dynamical state of the dust we can learn about the way dust is acquired.

In 11 of the 40 radio galaxies, all of which are FR II's, optical evidence for merging of galaxies is seen in the form of multiple nuclei or tails of emission. For only three of these radio galaxies (3C 293, 3C 327, and 3C 433) do the dust morphologies show strong distortions, also indicative of a recent disturbance of the galaxy. Of the other eight sources with optical evidence for merging, 3C 136.1 and 3C 306.1 have dust lanes with some faint dust structure around it, whilst 3C 171, 3C 180, 3C 196.1, 3C 275, 3C 284, and 3C 303.1 show no distortions in their dust lanes. (We note that each of these galaxies have a redshift $z \geq 0.2$ and therefore any extended diffuse dust structure may be missed. Also, for these six galaxies the evidence for the presence of dust is least strong; the presence of multiple nuclei can give the impression that the galaxy nucleus is obscured by a dust lane.)

Dust absorption features are seen in only 40 of the 120 radio galaxies (i.e., ~33%) investigated. In the remaining 80 radio galaxies dust may be present, distributed uniformly throughout the galaxy or clumped on scales below that at which we could detect it. Indeed, dust can be seen in emission using *IRAS* in many cases. We have investigated the entire sample for possible correlations between the presence of clumpy dust seen in absorption and other properties of the radio galaxy.

Examining the images of the radio galaxies convolved to a redshift of 0.5, as described in § 2.5, it is found that the fraction of radio galaxies in which clumpy dust is detected (and would still be detected if the galaxy were at redshift 0.5) is statistically indistinguishable from a flat distribution across redshift. Clumpy dust is also found equally often in FR I and FR II class radio galaxies, and also in a similar fraction of radio-quiet ellipticals (van Dokkum & Franx 1995). We searched for correlations between the clumpiness of the dust and other properties of the radio galaxies (radio power, redshift, radio size, environment, kinematics of the host galaxies gas, etc.), using the logarithm of the ratio $M_d/M_{D,IRAS}$ (or limits thereon) as an indicator of dust clumpiness. No significant correlations were found, although the strong correlations of both the *HST* clumpy dust mass detection limit and the detection limit of the *IRAS* observations meant that only an intrinsically narrow range of values could be studied, making it difficult to get significant results.

The reason for the dust to become clumpy does not appear to be found in the formation of the radio source (radio sources with otherwise similar properties are hosted by galaxies which both do and do not display dust), nor in the kinematics of the host galaxy, or environment of the radio source. It is not apparent, therefore, what the reason for the dust being clumpy to different extents in different galaxies is. If the galaxies have undergone recent mergers, then the conditions of this merger event could plausibly have an influence. For example, a stronger shock through the ISM in a high impact collision could lead to enhanced clumping of the dust. The settling times will be large (2–3 Gyr) in high angular momentum collisions, perhaps leading to the radio source being triggered before the dust has settled to the centers of the galaxy and become clumpy.
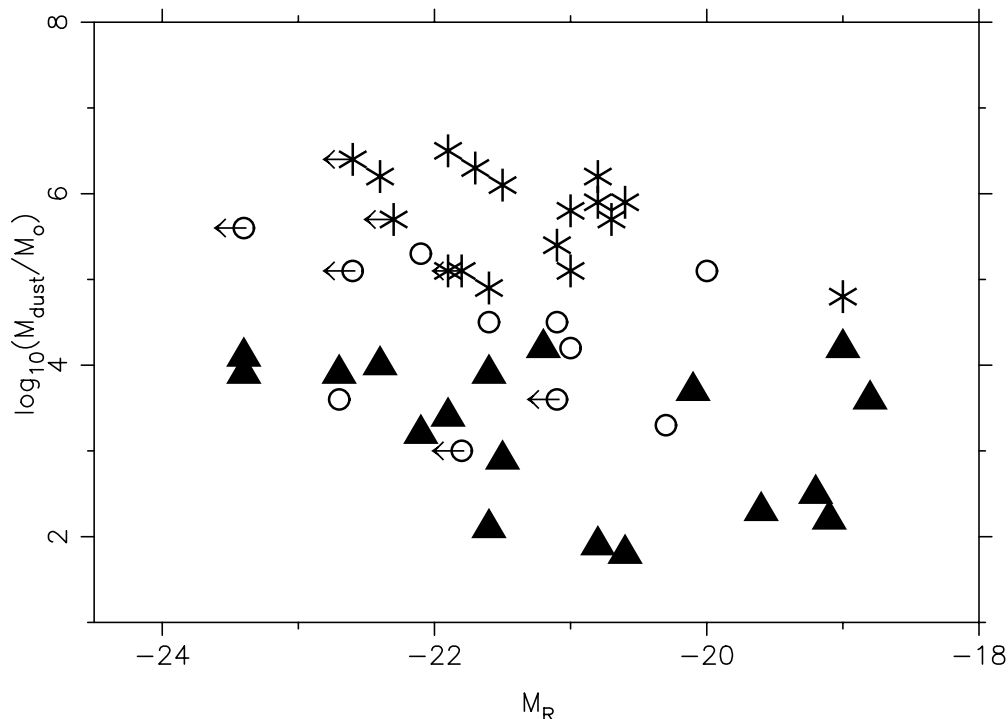
FIG. 50.—Logarithm of the estimated dust mass against the absolute magnitude. The open circles represent the 3CR FR I galaxies, the asterisks the 3CR FR II galaxies and the filled triangles represent the early-type galaxies from van Dokkum & Franx (1995).

5.2. The Nature of the Radio Source and Dust Association

Although it is not clear why clumpy dust should be present in some sources and not in others, our results together with previous work imply that, when clumpy dust is present, there must be a connection between the radio source and the dust. In a few cases there is strong evidence that the radio source interacts physically with the dust, e.g., the morphological alignment seen in 3C 305 suggests that the radio jet plows through the dust and disperses it along the radio jet axis. However, if we assume that the observed distribution of Δ is a reflection of the true distribution of position angle differences, then for most of the sources in which a central dust disk forms the radio jet is positioned roughly perpendicular to the dust disk/lane.

Three plausible scenarios can be considered for the interaction between the clumpy dust and the radio source:

1. The dust "feels" the radio and adapts to its force, being moved into a preferred plane.

2. The dust and gas are the trigger for the radio source, and because of the fueling of the black hole, the radio source will be perpendicular to the direction of accretion, i.e., the plane of the dust disk.

3. Both clumpy dust and black hole spin axis are both strongly coupled to the large-scale surroundings (West 1994).

The many differences in the dust properties between FR I's and FR II host galaxies are likely to be linked to the very different properties of the radio sources. Many other differences are also known between the two host galaxy types, such as differences in the optical magnitudes and environments, and in the emission line gas properties and kinematics. Three scenarios which have been proposed for the differences between FR I and FR II sources are that:

1. There is a difference in the origin of the accreting material, it being internal, or due to close encounters for FR I's and external (through violent mergers) for FR II's.

2. The central engine has different properties (accretion rates, spin of the black hole).

3. FR II sources evolve into FR I sources with time.

If scenario 3 were true, then the mass of clumpy dust in the FR IIs would have to decrease by a factor of about 10 as the radio source ages and evolves into an FR I. This should be seen in a statistical sense as a difference in the dust mass between small (young) and large (old) FR II radio sources. The lack of any correlation between the radio size of FR II sources and their dust mass therefore argues against scenario 3. The current data cannot say anything about scenario 2, but would be consistent with scenario 1, with the difference in FR class being determined by the origin of the accreting material.

5.3. Conclusions

We examined 40 images of 3CR radio galaxies that show evidence for the presence of clumpy dust. Model absorption maps were made by dividing the original image by a smooth galaxy model. We found that 40 out of 120 radio galaxies show absorption indicative of the presence of clumpy dust. The remaining 80 radio galaxies may have more smoothly distributed dust in them as seen in emission using IRAS. No differences in properties between the radio galaxies with clumpy dust and without clumpy dust are found.

Considering only the radio galaxies that have dust in clumps, there is a tendency for the dust major axis to be perpendicular to the radio source. A strong correlation between this position angle difference and FR-type exists. For FR I galaxies, the dust is found mostly in sharply

defined disks concentrated into the inner 2.5 kpc of the galaxy, with the dust major axis perpendicular to the radio jet in almost all cases. For the FR II galaxies a wide variety of dust morphologies is seen, from sharply defined disks to filamentary and patchy dust all throughout the galaxy. The correlation between the dust and radio position angles is only strong if attention is limited to those sources that have their dust in disks concentrated close (<2.5 kpc) to the nucleus.

Masses of the clumpy dust were derived using the model absorption maps and compared to the dust masses found in early-type (radio-quiet) galaxies. We find that high dust masses are more likely to be found in the 3CR radio galaxies, with the highest dust masses found in FR II radio galaxies. Dust clearly plays an important role in the evolution of radio galaxies.

In a future paper we will present color information of most of the radio galaxies presented in this paper. This will help us get more quantitative information about the properties of the dust and help entangle questions about the connection between the dust and radio source.

REFERENCES

Akujor, C. E., Spencer, R. E., Zhang, F. J., Davis, R. J., Browne, I. W. A., & Fanti, C. 1991, MNRAS, 250, 215
Barthel, B. P., Schilizzi, R. T., Miley, G. K., Jagers, W. J., & Strom, R. G. 1985, A&A, 148, 243
Baum, S. A., Heckman, T. M., Bridle, A., van Breugel, W. J. M., & Miley, G. K. 1988, ApJS, 68, 643
Baum, S. A., et al. 1997, ApJ, 483, 178
Baum, S. A., Zirbel, E. L., & O'Dea, C. P. 1995, ApJ, 451, 88
Bennett, A. S. 1962, MmRAS, 68, 163
Black, A. R. S., Baum, S. A., Leahy, J. P., Perley, R. A., Riley, J. M., & Scheuer, P. A. G. 1992, MNRAS, 256, 186
Burns, J. O., Schwendeman, E., & White, R. A. 1983, ApJ, 271, 575
de Koff, S., Baum, S. A., Sparks, W. B., Biretta, J., Golombek, D., Macchetto, F., McCarthy, P., & Miley, G. 1996, ApJS, 107, 621
Fanaroff, B. L., & Riley, J. M. 1974, MNRAS, 167, 31
Fraix-Burnet, D., Golombek, D., & Macchetto, F. D. 1991, AJ, 102, 562
Ge, J., & Owen, F. N. 1994, AJ, 108, 1523
Golombek, D., Miley, G. K., & Neugebauer, G. 1988, AJ, 95, 26
Goudfrooij, P. 1994a, Ph.D. thesis, Amsterdam
————. 1994b, MNRAS, 271, 833
Hansen, L., Norgaard-Nielsen, H. U., & Jorgensen, H. E. 1985, A&A, 149, 442
Heckman, T. M., Miley, G. K., Balick, B., van Breugel, W. J. M., & Butcher, H. R. 1982, ApJ, 262, 529
Heckman, T. M., van Breugel, W. J. M., & Miley, G. K. 1984, ApJ, 286, 509
Hildebrand, R. D. 1983, QJRAS, 24, 267
Howarth, I. D. 1983, MNRAS, 203, 301
Jackson, N., Sparks, W. B., Miley, G. K., & Macchetto, F. 1995, A&A, 296, 339
Jaffe, W., Ford, H., Ferrarese, L., van den Bosch, F., & O'Connell, W. 1996, ApJ, 460, 214
Jedrzejewski, R. I. 1987, MNRAS, 226, 747
Kotanyi, C. G., & Ekers, R. D. 1979, A&A, 73, L1
Laing, R. A., & Bridle, A. H. 1987, MNRAS, 228, 557
Laing, R. A., Riley, J. M., & Longair, M. S. 1983, MNRAS, 204, 151
Leahy, J. P., Black, A. R. S., Dennett-Thorpe, J., Hardcastle, M. J., Komissarov, S., Perley, R., Riley, J. M., & Scheuer, P. A. G. 1997, MNRAS, 291, 20
Leahy, J. P., & Perley, R. A. 1991, AJ, 102, 537
Leahy, J. P., Pooley, G. G., & Riley, J. 1986, MNRAS, 222, 753
Leahy, J. P., & Williams, A. C. 1984, MNRAS, 210, 929
Mack, K., Klein, U., O'Dea, C. P., & Willis, A. G. 1997, A&AS, 123, 423
Mantovani, F., Junor, W., Fanti, R., Padrielli, L., Browne, I. W. A., & Muxlow, T. W. B. 1992, MNRAS, 257, 353
Martel, A., et al. 1999, ApJS, 122, 81
Morganti, R., Killeen, N. E. B., & Tadhunter, C. N. 1993, MNRAS, 263, 1023
Neff, S. G., Roberts, L., & Hutchings, J. B. 1995, ApJS, 99, 349
Pedlar, A., Ghataure, H. S., Davies, R. D., Harrison, B. A., Perley, R., Crane, P. C., & Unger, S. W. 1990, MNRAS, 246, 477
Poggianti, B. M. 1997, A&AS, 112, 399
Sadler, E. M., & Gerhard, O. E. 1985, MNRAS, 214, 177
Steinman-Cameron, T. Y. 1991, in Warped Disks and Inclined Rings around Galaxies, ed. S. Casertano, P. Sackett, & F. Briggs (Cambridge: Cambridge Univ. Press), 131
van Breugel, W., Heckman, T., Butcher, H., & Miley, G. 1984, ApJ, 277, 82
van Dokkum, P. G., & Franx, M. 1995, AJ, 11, 2027
Verdoes Kleijn, G. A., Baum, S. A., de Zeeuw, P. T., & O'Dea, C. P. 1999, AJ, in press (astro-ph/9909256)
West, M. J. 1994, MNRAS, 268, 79
Wrobel, J. M., Condon, J. J., & Machalski, J. 1998, ASP Conf. Ser. 144, Radio Emission From Galactic and Extragalactic Compact Sources, ed. J. Anton Zensus, G. B. Taylor, & J. M. Wrobel (San Francisco: ASP), 209
Xu, W., Readhead, A. C. S., Pearson, T. J., Polatidis, A. G., & Wilkinson, P. N. 1995, ApJS, 99, 297
Zirbel, E. L., & Baum, S. A. 1995, ApJ, 448, 521